EUROPEAN ORGANIZATION FOR NUCLEAR RESEARCH

CERN PH–EP/2004–050
19 August 2004

# Novel Geometrical Concept of a High Performance Brain PET Scanner - Principle, Design and Performance Estimates

J. Séguinot[a,b], A. Braem[b], E. Chesi[b], C. Joram[b*], S. Mathot[b], P. Weilhammer[b], M. Chamizo Llatas[c], J.G. Correia[d], M. Ribeiro da Silva[e], F. Garibaldi[f], R. De Leo[g], E. Nappi[g], F. cOrsi[h], A. Dragone[h], F. Schoenahl[i] and H. Zaidi[i]

[a]Collège de France, Paris, France

[b]CERN, PH Department, Geneva, Switzerland

[c]University of Geneva, Department of Corpuscular and Nuclear Physics, Geneva, Switzerland

[d]Instituto Tecnolgico e Nuclear, Sacavém, Portugal

[e]Centro di Fı́sica Nuclear da Universidade de Lisboa, Portugal

[f]Instituto Superiore di Sanita, Roma, Italy

[g]INFN, Sezione di Bari, Italy

[h]DEE, Politecnico di Bari, Bari, Italy

[i]Division of Nuclear Medicine, Geneva University Hospital, Geneva, Switzerland

We present the principle, a possible implementation and performance estimates of a novel geometrical concept for a high resolution positron emission tomograph. The concept, which can for example be implemented in a brain PET device, promisses to lead to an essentially parallax free 3D image reconstruction with excellent spatial resolution and constrast, uniform over the complete field of view. The key components are matrices of long axially oriented scintillator crystals which are read out at both extremities by segmented Hybrid Photon Detectors. We discuss the relevant design considerations for a 3D axial PET camera module, motivate parameter and material choices, and estimate its performance in terms of spatial and energy resolution. We support these estimates by Monte Carlo simulations and in some cases by first experimental results. From the performance of a camera module, we extrapolate to the reconstruction resolution of a 3D axial PET scanner in a semi-analytical way and compare it to an existing state-of-the art brain PET device. We finally describe a dedicated data acquisition system, capable to fully exploit the advantages of the proposed concept. We conclude that the proposed 3D Axial concept and the discussed implementation is a competitive approach for high resolution brain PET. Excellent energy resolution and Compton enhanced sensitivity are expected to lead to high quality reconstruction and reduced scanning times.

*Keywords: Positron Emission Tomograph; PET; Hybrid Photon Detector; HPD; Scintillator.*

## 1. Introduction

We propose a novel geometrical concept[2] of a positron emission tomograph (PET) which aims at an optimized performance in terms of sensitivity, spatial resolution and image constrast. The goal is to maximize the detection efficiency for annihilation photons and, at the same time, to push the spatial resolution towards the physical limits inherent to the annihilation process. Those are determined by the positron range in the organic tissue and the non-collinearity of the 511 keV annihilation photons. A further goal is to achieve an optimized ratio of signal to noise, which finally translates into image contrast.

Our proposal is motivated by the demand of the medical imaging community, expecting comprehensive and high quality information for a more precise and certain assessment of malign tumours or major neurodegenerative diseases, combined with an improved comfort for the patient during the examination. This implies a significant shortening of the scanning time, or in some cases a reduced injected radiotracer dose.

PET is widely recognized as the best available molecular non-invasive diagnosis technique sensitive to tracer concentrations on the picomole level [1–5]. It provides access to metabolic and kinetic parameters of a particular molecular process and hence not only allows the detection of major deseases but also the follow-up of their treatment.

In recent years there has been significant progress in PET instrumentation, data quantification and image reconstruction [6–8]. PET instrumenation is benefitting of the ongoing development of new particle physics detector components like inorganic scintillators of high density, atomic number and light yield as well as photodetectors like MAPMT, APD and HPD[3]. A similar impact have come through advances in microelectronics, which led to highly integrated CMOS front-end circuits, fast data acquisition processors and ultra rapid FPGAs (Field Programmable Gate Arrays).

**State of the art in PET instrumentation**

One of the most recent and powerful PET devices [9,11] is the so-called High Resolution Research Tomograph (ECAT-HRRT) [10,12,13], developed by CPS-Innovations[4], which we consider as reference for the new generation of PET scanners. Its performance approaches the physical limits which are intrinsic to a design concept based on the radial arrangement of scintillators blocks, read out with PMTs. The centroid method (Anger logic) and the phoswich technique are used to reconstruct the interaction point of the annihilation photons in the crystal [14]. The ECAT-HRRT consists of octagonal arrangements (42.4 cm face-to-face) of phoswich scintillator block detectors, made of two layers of 64 small LSO crystals (each $2.1 \times 2.1 \times 7.5$ mm$^3$) with 2 different decay times ($\Delta\tau \approx 7$ ns). The total active length is therefore 15 mm. The crystals are oriented normal to the octagon sides, hence essentially pointing in radial direction. Each block is readout by an arrangement of 4 standard PMTs (diameter 19.6 mm), which are optically coupled to the block by means of a light guide which spreads the light from the individual crystals over all 4 PMTs. The centroid corresponds to the true interaction point of the annihilation photon, in case of conversion by photoelectric effect, or to the energy averaged mean position of the interaction in case Compton scattering in the detector is involved.

The phoswich technique is able to roughly halve the uncertainty of the depth of interaction (DOI) and hence significantly reduces the parallax error. However, the phoswich approach is still only a compromise between the maximum crystal length, which can be tolerated for parallax error reasons, and the minimum length which is required to achieve high detection efficiency. Moreover the phoswhich approach demands a delicate pulse shape discrimination of the analogue signal delivered by the PMTs in order to identify the hit crystal layer. The readout electronics becomes unavoidably more complex and possibly

*Corresponding author, Christian.Joram@cern.ch

[2]Patent application filed under PCT/EP02/07967, international publication number WO 2004/008177 A1.

[3]MAPMT = Multi Anode Photomultiplier Tube, APD = Avalanche Photodiode, HPD = Hybrid Photon Detector.

[4]CPS Innvoations, Knoxville, TN, USA

limits the data acquisition rate.

The centroid method is intrinsically precise, but the granularity of the Anger logic readout remains relatively poor. It is therefore impossible to track annihilation photons which undergo one or two Compton scatterings in the same detector block. They can not be rejected as Compton events if the total deposited energy falls inside the energy acceptance window, and hence degrade the spatial resolution. In the case of the HRRT, about 40% of all events fall in this category. A large fraction of these Compton events create energy deposition in both phoswich layers and can in principle be rejected by a careful pulse shape and energy discrimination.

We conclude that a substantial improvement of the PET imaging technique requires a different concept which is able to increase at the same time sensitivity, spatial resolution and background discrimination. The ultimate performance requires a thick and finely segmented array of high density and high Z scintillating crystals, *individually* read out. Precise 3D reconstruction of the photon interactions in such a crystal matrix allows to track annihilation photons which undergo photoelectric or Compton scattering. Compton events, if unambiguously reconstructed, are able to enhance the sensitivity without degrading image quality or contrast. Finally it is the patient who profits from this in form of a lower injected radioactive dose or a reduced scanning time which not only improves the patient's comfort but also lowers the risk of patient movements during the scan.

Co-registration of the metabolic activity by PET with a precise imaging of the anatomic structure using gamma or X-ray computed tomography (CT) is a proven way of improving the diagnostic potential. This multimodality approach allows, by means of image fusion, for an accurate localisation of the detected radiotracer emission pattern. In addition the CT information can be used to correct for the gamma ray attenuation in the tissue, an effect which still leads to false estimation of the source intensity and hence prevents a precise quantification of PET information.

Several developments projects in PET instrumentation have been proposed or are currently under design or test. To our knowledge, most of them rely on the classical radial scintillator arrangement.

In this article we describe in detail a concept for a brain PET scanner based on long scintillating crystals which are axially oriented. This concept allows to achieve the maximum detection efficiency and at the same time provides precise 3D and parallax free reconstruction of photoelectric and Compton events over the full field of view (FOV). The spatial resolution in the transaxial plane does not depend on the source position and matches the intrinsic physical limitations due to the range of the positron in the organic tissue and the non-collinearity of the 511 keV annihilation photon pair.

The axial arrangement of the scintillating crystals is a natural and straightforward idea to suppress the parallax error which is inherent to all radial geometries. As we discovered only recently, essential parts of the concept described in this article, were already proposed in 1988 [15], however the proposal seemed pre-mature given the state-of-the-art of scintillating crystals and photodetectors at that time. Matrices of BGO crystals ($3 \times 5$ mm$^2$) of 50 mm length were intended to be read out on both ends by position sensitive PM tubes with crossed wire anodes. Such a readout does not permit to track photon interactions in the crystal matrix and therefore leads to reconstruction ambiguities for Compton interactions. In addition the modest light yield of BGO crystals compromised the achievable reconstruction resolution in the axial direction. The authors have not pursued this development much further, which probably also explains why it is not mentioned in recent review articles.

The paper is organized as follows: In Section 2 we describe the geometrical concept of a 3D Axial PET camera and its principle of operation. We discuss the key components, i.e. the long scintillators and the segmented Hybrid Photon Detectors. Section 3 is devoted to performance estimates in terms of spatial and energy resolution, based on analytical and Monte Carlo calculations. We also derive an estimate of the achievable image reconstruction resolution and compare it with the HRRT as an existing state-of-the-art

device. It is followed by a detailed discussion of the achievable sensitivity and its enhancement by exploiting events which involve Compton scattering in the crystal matrix (Section 4). In Section 5 we define a specific factor of merit, allowing an overall characterisation and benchmarking of the concept and its implementation. We finally (Section 6) present a conceptual study of a dedicated data acquisition system, which is able to exploit the advantages of the 3D Axial concept and its segmented photon detectors.

## 2. The 3D Axial geometry with HPD readout – A novel concept

In the following we describe in detail the principle and a possible implementation of a 3D Axial PET concept using HPDs for the readout of the scintillation light. The basic features of the concept have already been described briefly in recent publications [16–18].

### 2.1. Geometry and principle of operation

We propose detector modules which, for a brain PET scanner (Fig.1), could be arranged in a ring[5] of 35 cm inner free diameter. The distance between opposite crystals is in this case about 38 cm. A detector module (Fig. 2) consists of an array of long (15 to 25 cm depending on the scintillating material) optically polished crystals of small cross section ($3.2 \times 3.2$ mm$^2$), axially oriented and separated by 0.8 mm. Each array of $16 \times 13$ crystal bars is optically coupled at both ends to proximity focused Hybrid Photon Detectors made with a thin sapphire entrance window and a bi-alkali photocathode. The HPDs feature a Si sensor with a readout granularity of $4 \times 4$ mm$^2$ to accurately match the matrix configuration.

A large fraction of the scintillation light is trapped in the crystal bar and propagates by total internal reflection to the opposite extremities. In the transaxial (x, y) plane the highly segmented geometry provides, from the readout of the crystal bar address, accurate x,y coordinates with an excellent and uniform resolution (see Sect. 3), totally independent of the detector thickness. The line of record (LOR) reconstructed from a detected 511 keV annihilation photon pair is con-

[5] a second concentric ring with larger diameter can be added for full azimutal coverage.

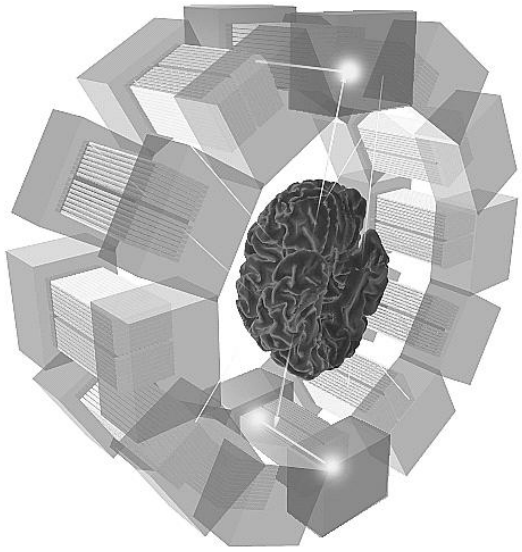

Figure 1. Schematic representation of a PET scanner based on 3D axial detector modules.

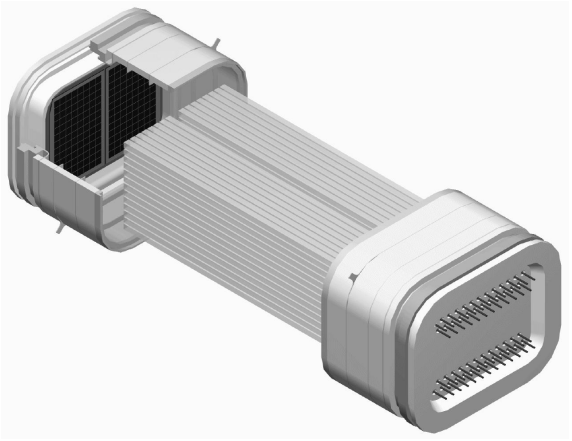

Figure 2. Drawing of a 3D axial detector module consisting of a matrix of 150 mm long crystals, read out by two HPDs.

sequently free of the parallax error intrinsic to the classic radial detector geometry. It results that the detector thickness can be increased up to 3 attenuation lengths which roughly double the sensitivity to photoelectric interactions compared to conventional detectors.

The fine segmentation in the transaxial plane allows the tracking of single or multiple Compton scatterings in the matrix. Their reconstruction, with a measurement of the total energy lost provides, unambiguously, an enhancement of the detection efficiency of 511 keV photons (Sect.4.1).

The measurement of the asymmetry of the amounts of light detected at the two crystal ends provides, with good accuracy, the determination of the axial coordinate z (see Sect. 3.1). The total deposited photon energy can be derived with good precision from the sum of the signals at the two ends, as the light attenuation during the propagation through the crystals can be corrected for.

As the critical angle for reflection at the interface with the sapphire window is higher than the maximum incident angle for LSO or $LaBr_3$ crystals, the number of photons transmitted onto the photocathode is only determined by the fraction of light trapped inside the bar and its attenuation in the crystal bulk. Because of the good match of the refractive indices at the wavelength of the scintillation light [6], the loss of photons by reflectivity at the interface crystal window is negligible.

The robustness of sapphire permits the use of a very thin (1.8 mm) window in order to limit the light spreading on the adjacent readout channels. Figure 3 is an illustration of a detector module designed for the demonstration of the concept with two round 5-in. HPDs. The gap of 0.8 mm between crystal bars is defined by means of nylon strings stretched at both ends on accurate frames without screening between bars to absorb the refracted light coming out of the crystal at the scintillation emission point.

[6] $n_{sapphire} = 1.798$ at 350 nm for $LaBr_3$ ($n = 1.88$); $n_{sapphire} = 1.780$ at 420 nm for LSO ($n = 1.82$)

### 2.2. The scintillator matrix: Fast Ce doped inorganic crystals

Table 1 summarizes the physical properties of Cerium doped inorganic fast scintillators already available, or still under development, which can be considered for an advanced PET system [19–29].

On the medium term, Cerium doped Lutetium Oxiorthosilicate (LSO: Ce)[7], Lutetium Yttrium Oxyorthosilicate (LYSO:Ce)[8] and Lanthanum Bromide ($LaBr_3$:Ce)[9] are the most promising candidates. LSO and LYSO have the significant advantage of a short attenuation length and a high photo fraction at 511 keV compared with $LaBr_3$. They are not hygroscopic and can be handled without special precaution contrary to $LaBr_3$. However the performance of LSO is much worse than the one of $LaBr_3$ in terms of light yield, energy resolution and linearity of the response with energy. The peak wavelength of the scintillation light at 358 nm for the $LaBr_3$, compared to 420 nm for LSO, leads to a higher detection efficiency due to the blue-enhanced sensitivity characteristics of standard (bi-alkali) photocathodes (see Sect. 2.3.2).

The use of long crystal bar (15 to 25 cm) in one or two pieces optically coupled, imposes more

[7] CTI PET system (Knoxville, TN, USA)
[8] Photonic Material (Scotland)
[9] Saint Gobain – Bicron (France)

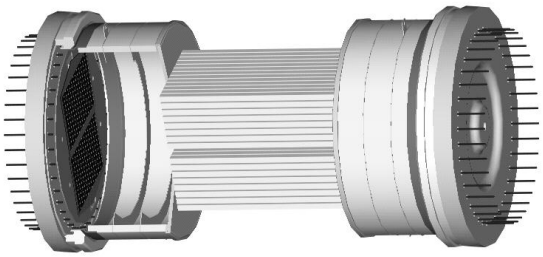

Figure 3. Prototype of a 3D Axial detector module for proof of principle measurements. The scintillator matrix is composed of already available YAP crystals of dimensions $3.2 \times 3.2 \times 100$ mm$^3$.

Table 1
Properties of scintillation crystals used for PET.

| Scintillator | BGO[1)] | LSO[2)] | LYSO[3)] | GSO[4)] | LuAP[5)] | LaBr[6)] | YAP[7)] |
|---|---|---|---|---|---|---|---|
| Density (g/cc) | 7.1 | 7.4 | 7.1 | 6.7 | 8.3 | 5.3 | 5.4 |
| Light yield (photons/keV) | 9 | 27 | 32 | 8 | 10 | 61 | 21 |
| Effective Z | 75 | 66 | 64[*)] | 60 | 65 | 46.9 | 31.4 |
| Principal decay time (ns) | 300 | 42 | 48 | 30-60 | 18 | 35 | 25 |
| Peak wavelength (nm) | 480 | 420 | 420 | 440 | 365 | 358 | 370 |
| Index of refraction | 2.15 | 1.82 | $\approx 1.8$ | 1.95 | 1.95 | 1.88 | 1.94 |
| Photofraction at 511 keV(%) | 41.5 | 32.5 | 34.4[**)] | 25 | 30.6 | 15 | 4.5 |
| Attenuation length at 511 keV(cm) | 1.04 | 1.15 | 1.12 | 1.42 | 1.05 | 2.13 | 2.19 |
| Energy resolution[***)] at 662 keV (%) | 7.9 | 8 | 7.1 | 6.9 | 10 | 2.9 | 3.8 |
| Hygroscopic | No | No | No | No | No | Yes | No |

[1)]$Bi_4Ge_3O_{12}$; [2)]$Lu_2SiO_5$:Ce; [3)]$LuYSiO_5$:Ce; [4)]$Gd_2SiO_5$:Ce; [5)]$LuAlO_3$:Ce; [6)]$LaBr_3$:Ce; [7)]$YAlO_3$:Ce
[*)]Calculated; [**)]Result of simulation with Geant4; [***)] $\Delta E/E$ FWHM.

constraints for the fabrication (growing, cutting and polishing) and for the mechanical (robustness) and the optical (surface quality) properties. The production of crystals of this length is technically feasible, however it may have an impact on the cost.

The adjustment and the calibration of the light attenuation in the crystal bars is a key parameter since they determine the reconstruction accuracy of the axial coordinate and the energy resolution. These aspects are discussed in sect. 3 and 4 for LSO and $LaBr_3$ crystals.

Studies with LYSO samples have revealed promising characteristics. They show an energy resolution comparable to LSO, but, in contrast to LSO, the response scales linearly with energy. Producers claim that a photon yield of $35 \cdot 10^3$ photons/MeV is attainable (LYSO with $31 \cdot 10^3$ photons/MeV is already available from St. Gobain). If these performances are confirmed in future, LYSO would be a very good candidate.

Ce doped LuAP [30] crystals can presently not be used because of their low light yield (about $10^4$ ph/MeV) despite very good physical properties especially their short decay time (18 ns) compared to LSO (42 ns). However new developments have proven that a photon yield of $20 \cdot 10^3$ ph/MeV is possible, opening interesting perspective on a longer time scale.

### 2.3. The PET HPD - a Hybrid Photon Detector with enclosed VLSI readout electronics

HPDs [31–33] are unique photon detectors for medical imaging applications compared to standards PMTs, MAPMTs and commercially available APDs. An HPD consists of a vacuum envelope with a transparent entrance window on which a semitransparent photocathode is evaporated. A photoelectron, ejected from the photocathode (on potential $U_C$), is accelerated towards the segmented silicon anode (ground potential), in which, on impact, a large number of electron-hole pairs and hence a detectable signal is produced. The gain of the HPD is $M \equiv N_{e-h} \approx e \cdot U_c/W_{Si}$ with $W_{Si} = 3.6$ eV being the energy needed to create an electron hole pair in silicon.

HPDs combine the sensitivity to single photons, known from standard vacuum phototubes, with the exceptional spatial and energy resolution and the great design flexibility (size and geometry) of silicon sensors. Photon detectors of large sensitive area with a high readout granularity can be fabricated. The multiplexed VLSI front-end readout electronic is encapsulated in the detector body. This minimizes the effective capacitance to a few pF per channel and hence improves the signal characteristics (bandwidth and noise). The number of connecting lines (vacuum feedthroughs) required for the data acquisition is reduced by about a factor of 5 with respect to the

number of channels.

APDs [34,35] are the most promising competitors to be compared with HPDs. Commercially available APDs are mostly mono channel photon detector of about 20 $mm^2$ acceptance. They are insensitive to axial and transversal strong magnetic fields. Proximity focused HPDs can be operated in strong magnetic fields, as long as the field direction is aligned with the tube axis. Axial magnetic fields have even the beneficial effect of reducing the so-called point spread function, which is a consequence of the angular and energy distribution of the photoelectrons at emission from the photocathode, and therefore lead to an improved spatical resolution.

APD arrays [36–39] of 32 channels (typically $2 \times 2$ $mm^2$/channel) have been developed. Their granularity, as for MAPMTs, is usually fixed by the market. The configuration of the scintillator matrix has to be adapted to the available readout granularity, while HPDs can be designed and built to match a crystal array with optimized geometry.

The sensitivity of HPDs is determined by the quantum efficiency of the semi transparent bialkali photocathode which, at 400 nm, is about 30 to 50% lower than the quantum efficiency of reverse [40] and high capacitance APDs[10], respectively.

HPDs operated at a moderate acceleration voltage of $U_C = 12$ kV have a gain of $M \approx 3 \cdot 10^3$, well adapted to the performances of modern front-end electronics with an Equivalent Noise Charge ($NEC$) of $< 2 \cdot 10^3$ electrons. If required, they can be operated up to 20 kV increasing the gain to $5.5 \cdot 10^3$ without lack of performances. The gain is achieved in a single stage dissipative process and is therefore practically free of avalanche related excess fluctuation. Consequently, the Excess Noise Factor $ENF$, which enters in the energy resolution of the detection system (see Section 3.2) is only 1.09 compared to $1.4 \pm 0.05$ for PMTs. The small excess noise of an HPD is caused by those ≈20% of photoelectrons which are back scattered from the silicon sensor and deposit only partially their kinetic energy.

[10] cf. data sheets of Hamamatsu APDs

Intrinsic to their principle of operation, the linearity of the response with the incident light (or energy deposition in the crystal) is excellent. Gain and signal characteristics are unaffected by variations of the detector temperature.

In principle, APD can achieve gains up to $10^3$, but, in practice, their use is limited to gains of few $10^2$ for an acceptable stability ($1/M \times dM/dV = 3.1\%/V$) with the operating voltage $V$. Moreover their $ENF$ increases linearly with the gain [41] and usually varies from $ENF = 2$ or 3 for $M = 50$ to $ENF = 9$ for $M = 10^3$. Therefore, even with a gain of 50, the energy resolution with an APD is 50 to 70% worse compared to a HPD operated at gains of 3 to $5 \times 10^3$.

The temperature dependence ($1/M \times dM/dT$) of APDs is about -2%/K requiring cooling, and their dark current at room temperature is of the order of few nA for $M = 50$, instead of few tens of pA/pad for HPDs independently of the gain.

The use of APDs at low gain finally requires very low noise front-end electronics; a challenging development if fast response is required with stray capacitances in the 100 pF range.

A last and important advantage of HPDs is the possibility of reading out the induced signal on the non-segmented Si sensor back plane (the side on which the accelerated photoelectrons hit the sensor) providing a fast measurement of the total energy deposited in the full Si sensor, i.e. in the total crystal matrix coupled to the HPD. This unique feature of the HPDs allows for a simple and fast gamma energy discrimination - without need to readout the individual detector channels. The back plane information can be used to discriminate annihilation photons which underwent Compton scattering in the organic tissue of the body or in the crystal matrix with incomplete energy deposition. Moreover, the fast back plane signals can be used to find coincident detector modules with a time resolution of potentially 5 ns (see Section 6).

We believe that HPDs are at the moment the best performing and flexible position sensitive photon detectors for our PET concept.

A dedicated plant has been designed and built at CERN to produce HPDs up to 10 in diameter, as well as all the various technologies needed

to prepare the components [42–45]. The prototype of a proximity focused HPD for PET applications which we describe below has entirely been designed, developed and fabricated in this framework.

### 2.3.1. Design of the PET-HPD

The prototype proximity focused HPD developed at CERN is a round photodetector with a bialkali photocathode deposited on a thin (1.8 mm) flat sapphire entrance window of 105 mm diameter (see drawing and photograph in Figs. 4 and 5). The total length of the HPD is 67 mm. A cross section of the HPD is shown in Fig. 6 with the electron optical configuration simulated using the SIMION[11] code). The window is sealed to a

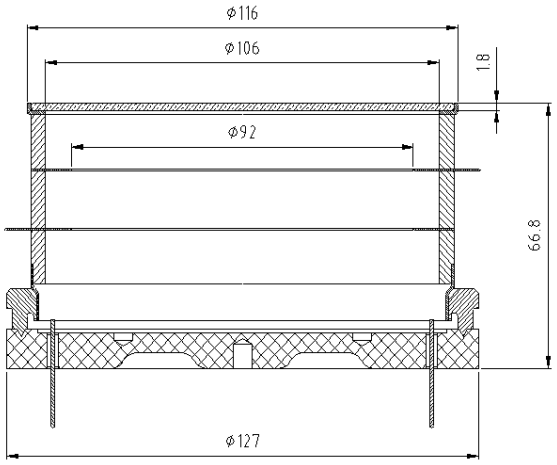


Figure 4. Cross-section of the proximity focused prototype HPD.

metallic ring made of niobium which assures the connection for the photocathode polarization. A set of two electrodes in niobium (0.7 mm thick) inserted in between cylindrical alumina spacers (ceramic) guarantee a precise 1:1 electron optical image transfer (i.e. proximity focusing) from the photocathode onto the silicon sensor. At the base of the body a skirt in kovar is welded to a stainless steel flange equipped with a gold plated sharp edge knife. The ceramic rings, the sapphire window and the metallic components in niobium and kovar are joint by means of active high temperature vacuum brazing. Details on the tube manufacturing and the indium sealing technology which is used to seal the tube in-situ after photocathode processing are given in [43].

The ceramic hybrid carrier which supports the sensor and the readout VATA chips is wire bonded to 40 vacuum feedtroughs of the base plate to provide the control and data lines connections to the data acquisition system.

The sensor consists of a 300 microns thick rectangular silicon plate with 16 x 13 pads implemented as $p^+n$ junctions, DC coupled to the front end electronic. The 208 pads of $3.96 \times 3.96$ mm$^2$ with a gap of 80 microns match precisely the crystal matrix configuration. The pad size is larger than the crystal bar cross section ($3.2 \times 3.2$ mm$^2$)

Figure 5. Photograph of a proximity focused prototype HPD with round silicon sensor and integrated front-end electronics.

[11] SIMION 3D, Scientific Instruments Services Inc., Ringoes, NJ 08551, USA

to cope with the light spread on the photocathode due to the non-zero thickness of the HPD entrance window. This reduces the optical signal sharing with adjacent channels (see sect. 3.1.).

### 2.3.2. Performance of the prototype HPD

The proximity focused prototype HPD shown in Fig. 5 has been fabricated with the goal to study its electron optical and electrical properties, but also to validate the complete fabrication procedure. The HPD is equipped with a round 50 mm diameter Si sensor of 2048 pads of $1 \times 1$ mm$^2$ connected to 16 standard readout VA prime chips. This high granularity Si sensor allows to map out with high precision the electron optical properties. Fig. 7 shows the quantum efficiency of the photocathode of this first proximity focused prototype HPD. Once the cathode processing parameters are optimized, we expect a 10-15% higher sensitivity, similar to other HPDs, which we have fabricated. The window was scanned along diameters with a fine light spot (≈0.5 mm RMS) generated by a self triggered $H_2$ flash lamp. The resulting correlation between the radial position of the light spot and the centre of gravity of the charge distribution measured with the Si sensor exhibits, as shown in Fig. 8, a perfect 1:1 linear imaging within 1% deviation. The point spread function which describes the charge distribution for a point source is of the order of 0.3 mm (RMS). Fig. 11 shows for a fixed spot position the variation of the total charge measured in the image spot with the acceleration voltage. Above 10 kV, the variation is strictly linear. Below this value, i.e. at photoelectron energies below 10 keV, the energy loss in the dead $n^+$ layer implanted on the entrance bias side of the wafer increases and favours a minimum operating voltage of 12 kV.

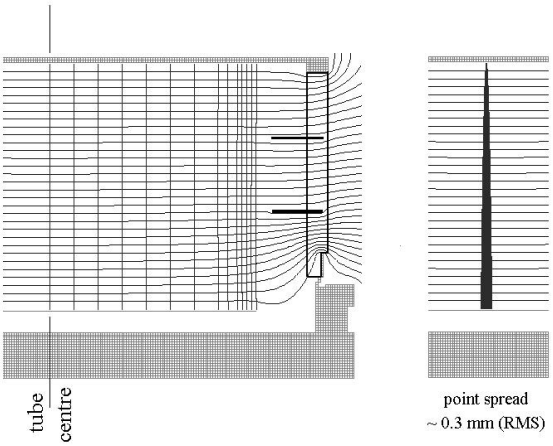


Figure 6. Cross-section of the proximity focused HPD as used in SIMION simulations. Left: Equipotentials and individual electron trajectories. Right: Bundle of electron trajectories from a point source allowing to determine the point spread function.

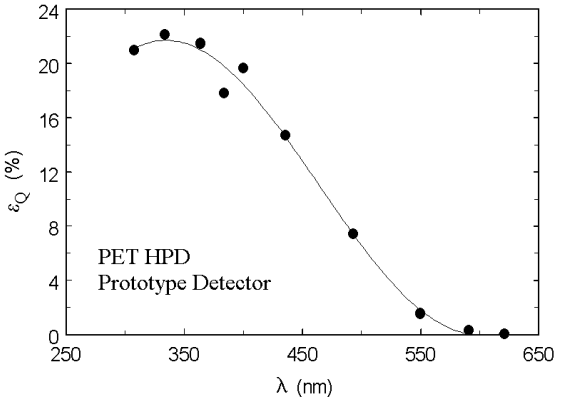


Figure 7. Measured quantum efficiency of the first prototype HPD.

### 2.4. The VLSI auto-triggering front-end electronic: the VATA–GP5

The Front end electronic is an important component of the PET concept designed to cope with high counting rates (up to 2 Mhz per module of 208 channels) and to be operated in a self triggering mode with a sparse readout of the data in order to optimize the data taking rate.

The VATA-GP5 chip is an optimized ASIC version of the existing VATA–GP3 and was devel-

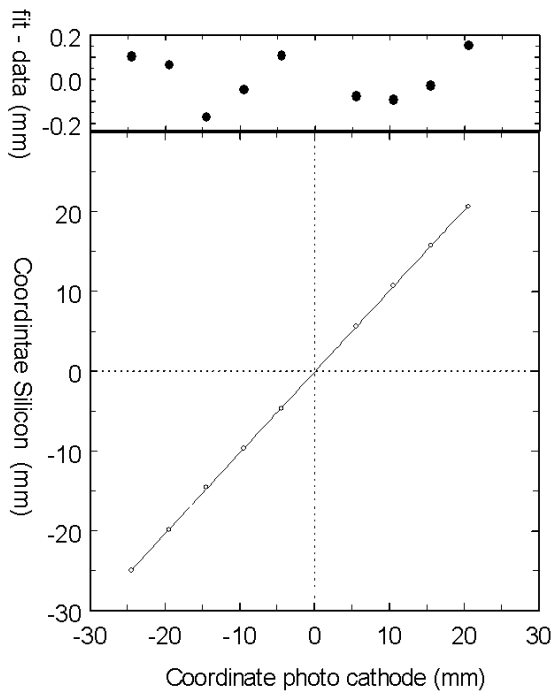


Figure 8. Measured relation between the photon coordinate at the photocathode and the photoelectron hit on the silicon sensor.

oped for the PAD HPD by IDEAS[12] in collaboration with CERN. For cost reasons the first prototype version was produced in 0.6 micron CMOS technology in order to validate the PET concept. In the future the chip should be implemented in deep submicron technology to increase the bandwidth and thus lead to optimal performance in terms of response speed, as require by a full PET system.

The VATA chips comprise 128 channels and is equiped with three readout modes: serial, sparse and sparse with adjacent channels.

Fig. 10 shows a block diagram of the VATA–GP5. The charge amplifier is optimized for a total detector capacitance of 5 to 7 pF and an input dynamic range of 1.2 pC for positive polarity.

[12]Ideas ASA, Norway

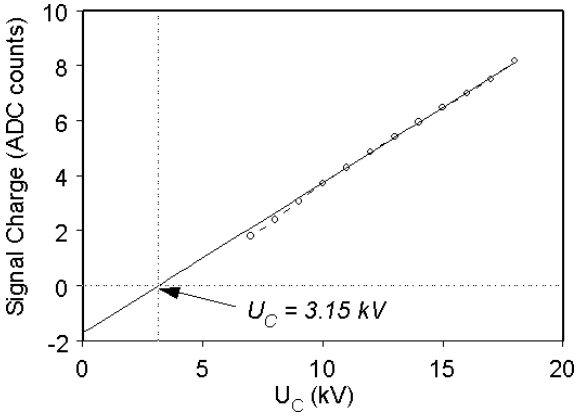


Figure 9. Pulse height (a.u.) versus cathode voltage (kV).

The analogue chain is a classical arrangement, where a Sample and Hold (S/H) signal is applied at the peaking time (150 ns) of the 'slow' shaper when a coincidence between a pair of modules is detected by an external logic (see Sect. 6). The hold signal stores the amplitude proportional to the input charge, to be later readout. The excellent linearity of the amplifier/shaper circuit is demonstrated in Fig. 11, where signals in the range from 0.06 to 1.25 pC were injected. Above 1 pC saturation effects become noticable, which are however due to the limited dynamic range of the ADC. The signal from the 'fast' shaper, of 40 ns peaking time, goes to a discriminator. A common threshold is applied to all channels. Individual channels can be trimmed by 4 bit DACs. Fig. 12 shows for two gain settings the excellent linearity of the discriminator in the range 0 to 120 fC. A timewalk compensation circuit is implemented at the input of each discriminator to suppress timewalk due to different signal amplitudes. The effect of the time walk compensation is shown in Fig. 13. Signals in the range from 60 to 160 fC are compensated within $\pm 5$ ns. The outputs of all the 128 discriminators are then ORed together providing a Fast Or signal ($FOR$) able to detect coincidences with an expected timing resolution of less than 10 ns. The VATA chip provides in

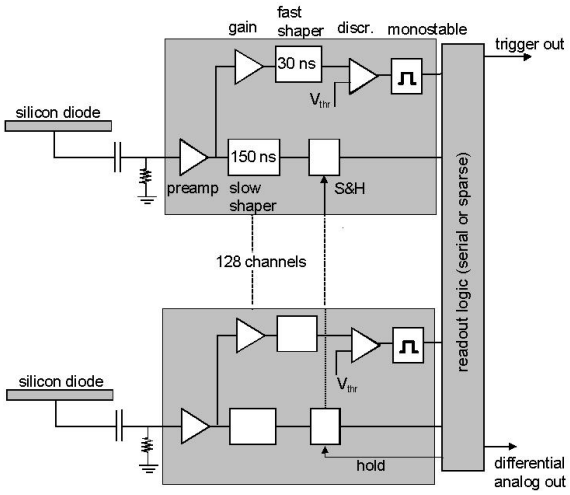


Figure 10. Schematic and simplified block diagram of the VATA-GP5 circuit.

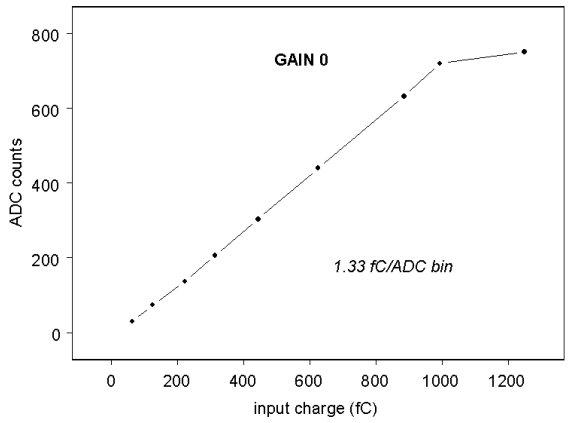


Figure 11. Response of the VATA-GP5 amplifier/shaper circuit to injected input charges from 0.06 to 1.25 pC .

addition a FOR signal with an amplitude proportional to the multiplicity of hit channels.

When a discriminator output is activated, the corresponding address of the channel is stored in a register. In sparse readout mode, if a *FOR* is detected, a veto signal blocks the generation of further *OR*s and only the analogue values of the hits channels with their address will be readout.

In normal PET operation the coincidence between two annihilation photons is established externally (see section 7) on the basis of the silicon backplane signals. On the contrary, if no coincidence is found, a reset signal is applied to the register in a minimum time delay ($< 12$ ns) in order to reduce the probability of having accidentals recorded when applying the common S/H signal. In addition, each discriminator output can be masked in case of malfunctioning of a channel.

The data acquisition speed is determined by the readout clock frequency which is currently limited to 20 MHz. The readout time is proportional to the number of hit channels plus three clocks per chip which are needed before to reach the first stored data.

If the sparse readout mode is an essential feature to maximize the data acquisition rate, the serial readout is needed to test the correct functioning of all the channels by injecting a calibrated pulse into each input, and register the pedestals for subtraction.

The lowest threshold of the fast discriminator ranges from 4 to 6 fC including the threshold spread after tuning with the channel trim DAC. It corresponds to about 5 sigmas of the shaper noise. With an HPD operated at 12 kV ($M = 3 \cdot 10^3$) a threshold setting of 5 fC would select annihilation photons (or recoil electrons) of energy higher than 10 to 12 keV for a scintillator matrix with LSO crystals. For $LaBr_3$ scintillators, the same threshold would provide a factor of about 1/3 on the minimum energy.

The equivalent noise charge ($ENC$) of the slow shaper is of about $2 \cdot 10^3$ electrons, a negligible contribution to the energy resolution ($< 0.1\%$) at 511 keV.

### 2.5. Configuration of a PET scanner

Fig. 14 shows a possible arrangement of 12 modules in a ring of 350 mm free inner diameter with rectangular HPDs. Those could be fabricated with a moderate upgrade of the tooling and production facilities. A full azimuthal cov-

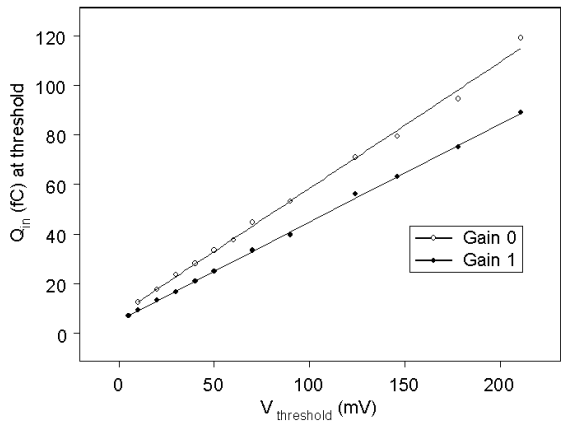


Figure 12. Characterization of the VATA-GP5 fast discriminator circuit with injected input charges from 0 to 120 fC.

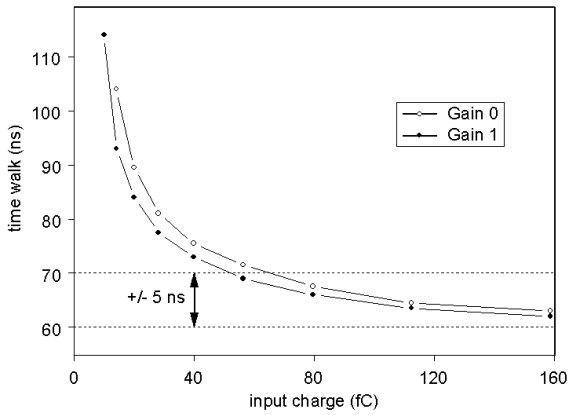


Figure 13. Characterization of the VATA-GP5 time walk compensation in the input charge range 10 to 160 fC.

erage would require a second concentric ring at larger radius.

## 3. Spatial reconstruction and energy determination

In the following we discuss the spatial and energy resolution which can be achieved with the axial concept. We also perform a direct comparison of certain characteristics between the axial and a conventional radial geometry.

### 3.1. Number of detected photoelectrons

The number of scintillations photons $N_{ph}$ generated by a 511 keV photon is $13.8 \cdot 10^3$ and $31.2 \cdot 10^3$ in LSO and $LaBr_3$, respectively. Ignoring initially the light absorption in the crystal bulk, the total light trapping and transport efficiency $\epsilon_{TT}$ has been determined by means of a microscopic photon transport Monte Carlo code (see below). As the light propagates by total internal reflections, almost perfect reflectivity (99.9% at each bounce) has been assumed. For square crystals of $3.2 \times 3.2$ mm$^2$, $\epsilon_{TT}$ has been found to be 0.614 (LSO) and 0.60 ($LaBr_3$). The small difference is due to the small difference in refractive index of the two materials.

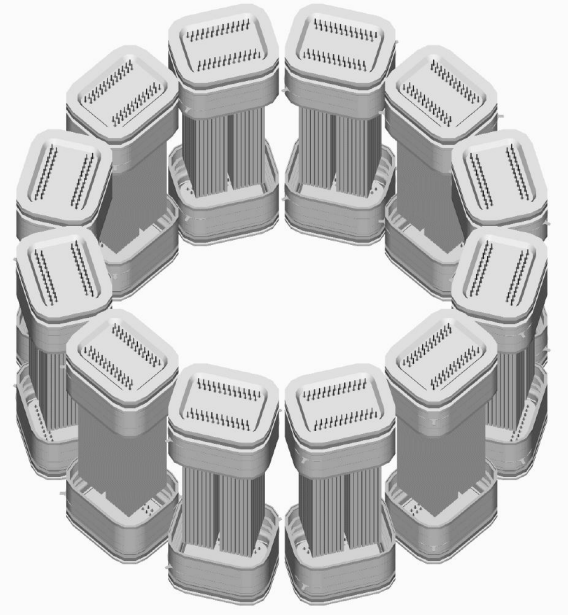

Figure 14. Possible arrangement of 3D Axial modules to a ring scanner.

With $\epsilon_Q$ being the quantum efficiency of the bialkali photocathode at the wavelength of the scintillation peak emission ($\epsilon_Q = 0.18$ for LSO and 0.25 for $LaBr_3$), the total number of photons detected ($\equiv N_{p.e.}$) at the two ends of the crystal is

$$N_{p.e.}(z) = N_1(z)+N_2(z) = \frac{N_o}{2}\cdot[e^{-z/\lambda}+e^{-(L_C-z)/\lambda}] \quad (1)$$

with

$$N_0 = N_{ph}\cdot\epsilon_Q\cdot\epsilon_{TT} = \begin{cases} 1525 \pm 39 & \text{(LSO)} \\ 4681 \pm 68 & (LaBr_3) \end{cases} \quad (2)$$

and $z$ being the axial coordinate of the interaction of the annihilation photon, with origin at one end of the crystal bar of length $L_C$.

The *effective* light absorption lenght $\lambda$ is different from the bulk absorption length $\lambda_b$ as it accounts for the real path length of the photons, which is increased due to the multiple bounces: $\lambda = k \cdot \lambda_b$. The geometrical parameter $k = z/\langle\text{path length}\rangle$ depends on the refractive index of the scintillator and has been determined for LSO and $LaBr_3$ in the M.C. code as $\approx 0.7$.

The spatial distribution of the photoelectrons over the segmented silicon sensor is shown in Fig. 15. About 70% of the photoelectrons of a hit crystal bar are detected by the associated sensor pad, while the rest is spread over the closest adjacent pads in a well defined pattern. Expressed in terms of energy, a 511 keV photon will deposit on an adjacent pad not more than the equivalent of about 30 keV.

### 3.2. Energy resolution

The energy resolution $R = \frac{\Delta E}{E}$ (FWHM), with which the photon energy can be measured, is the quadratic convolution of three contributions:

$$R = R_{sci} \oplus R_{stat} \oplus R_{noise} \quad (3)$$

The intrinsic resolution of the scintillator $R_{sci}$ due to material inhomogenities, impurities etc. was derived from ref. [22] by deconvoluting the statistical fluctuation term as $R_{sci} = 6.2\%$ and 1.2% for LSO and $LaBr_3$, respectively (see table 1). $R_{stat}$ accounts for the statistical fluctuation involved in the light generation, transport and detection process

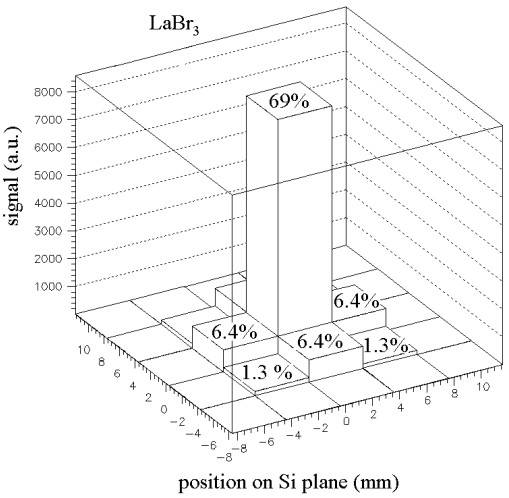


Figure 15. Simulated distribution of the hit map on the silicon sensor for the readout of a scintillator crystal centred over the cental Si pad.

$$R_{stat}(\text{FWHM}) = 2.35\sqrt{\frac{1.09}{N_{p.e.}}} \quad (4)$$

and includes the Excess Noise Factor of the HPD $ENF = 1.09$.

The contribution due to noise in the electronic detection chain including the photodetector (amplifier, shaper, ADC, ...) is negligible for HPDs. With an Equivalent Noise Charge (ENC) of about $10^3$ $e^-$, the noise term becomes

$$R_{noise}(\text{FWHM}) = \frac{2.35\cdot 10^3}{N_{p.e.}\cdot M} \approx 10^{-3} \quad (5)$$

where $M \approx 10^3$ is the gain of the HPD at $U_C =$ 12 kV.

The full energy resolution (acc. to eqn.3) at $E = 511$ keV is therefore 9% and 3.2% (FWHM) for LSO and $LaBr_3$, respectively.

### 3.3. Reconstruction of the interaction point of the annihilation photon

The coordinates of the photon interaction point in the transaxial (x, y) plane are derived from the

address of the hit crystal bars forming the scintillator matrix. The resolution $\sigma_x$ ($\sigma_y$) is determined by the cross section of the bar

$$\sigma_x = \sigma_y = \frac{s}{\sqrt{12}} \tag{6}$$

where $s$ = 3.2 mm is the width of the square crystals. The x and y coordinates of the photon interaction points can thus be localized with a precision of 2.2 mm (FWHM). Consequently the spatial resolution of the reconstructed positron annihilation point is in first order given by

$$\sigma_x^{rec.} = \sigma_y^{rec.} = \frac{s}{\sqrt{24}} \approx \frac{s}{2}(\text{FWHM}) \tag{7}$$

This approximation is strictly valid for a source centred in the transverse field of view, independent of the axial coordinate.

The axial coordinate $z$ of the photon interaction is derived from the measurement of the number of photoelectrons ($N_1$, $N_2$), detected at the two ends of the crystal bars.

$$z = \frac{1}{2}[\lambda \cdot ln(\frac{N_1}{N_2}) + L_C] \tag{8}$$

Error propagation w.r.t. the fluctuations of $N_1$ and $N_2$ (ignoring again the very small influence of electronics noise) leads to the measurement precision[13]

$$\sigma_z = \frac{\lambda}{\sqrt{2N_0}}[e^{z/\lambda} + e^{(L_c - z)/\lambda}]^{\frac{1}{2}} \tag{9}$$

and $\sigma_z^{rec} \approx \sigma_z/\sqrt{2}$.

### 3.4. Monte Carlo simulations of the light transport

The above mentioned Monte Carlo code allows to track scintillation photons individually from creation to detection. The code takes into account refraction and reflection at all optical interfaces (crystal/air, crystal/photodetector window), reflection and absorption losses as well as photodetector characteristics like quantum efficiency, point spread function and segmentation. The code allows to assess spatial and energy resolution and their variation with material and geometrical parameters and also provides an independent cross-check of the above derived analytical expressions.

#### 3.4.1. The influence of the bulk absorption length $\lambda_b$

The axial geometry with long scintillator crystals requires to choose the crystal bulk absorption length $\lambda_b$ in relation to the length of the crystal $L_C$, in order to define an optimal compromise between achievable energy and $z$-resolution.

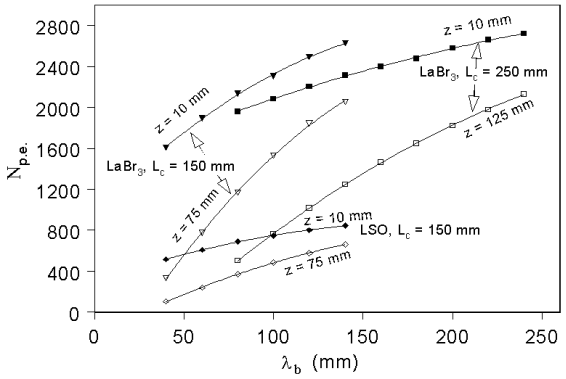


Figure 16. Variation of the number of detected photons with the bulk absorption length of the scintillator crystal.

Figures 16, 17 and 18 show simulation results for LSO ($L_C$ = 150 mm) and $LaBr_3$ crystals ($L_C$ = 150 and 250 mm), with $\lambda_b$ as free parameter. For every configuration light emission at $z_{em}$ = 10 mm and $z_{em} = L_c/2$ has been simulated, while $x_{em}$ and $y_{em}$ were varied uniformly $0 \leq x, y \leq 3.2$ mm. As good compromise appear 150 mm long crystals (LSO or $LaBr_3$) with $\lambda_b \approx 100$ mm. For 250 mm long $LaBr_3$ crystals $\lambda_b$ values around 140 mm give the best overall results. The lower light yield of LSO would lead to poor resolutions for 250 mm long crystals. This configuration was therefore discarded.

[13] eq. 9 ignores the contribution of pathlength fluctuations. Those are however accounted for by the M.C. calculations described in the next section.

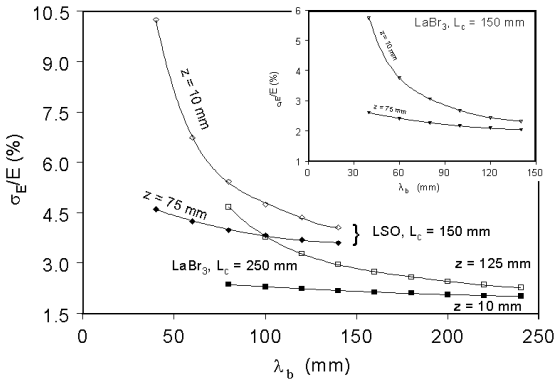


Figure 17. Dependence of the statistical term of the energy resolution ($E_\gamma = 511$ keV) on the bulk absorption length of the scintillator crystal.

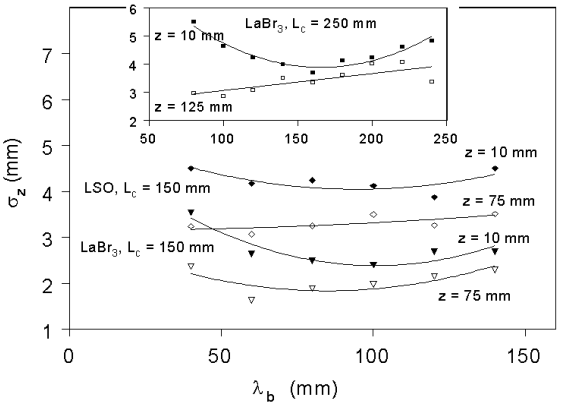


Figure 18. Dependence of the expected axial (z) resolution for single photons ($E_\gamma = 511$ keV) on the bulk absorption length of the scintillator crystal.

With these $\lambda_b$ parameters the achievable energy and spatial resolution has been investigated as function of the axial emission point $z_{em}$.

Fig. 19 shows the number of photoelectrons, detected by the two HPDs as a function of the emission point z. For comparison the results of the analytical calculation (dashed lines, acc. to equation 1) are shown together with the M.C. data, revealing a small but systematic discrepancy. The analytical calculations are made with a constant value of $\epsilon_{TT}$, while in reality $\epsilon_{TT}$ depends slightly on the emission position. This is a pure geometrical effect and is due to the increasing fraction of scintillation photons which can directly hit the photodetector without prior reflection from the crystal side faces. The maximum difference is about 5%. The number of detected photons and the z coordinate depend strongly on the effectice light absorption length $\lambda$ (see equations 1 and 8). For an accurate reconstruction of the energy and interaction point of the annihilation photon, the effective light absorption length $\lambda$ of all crystal bars needs to be determined experimentally, in order to cope with production related variations. In the annex we describe a simple procedure to measure $\lambda$ with a precision on the percent level. The statistical term of the energy resolution ($\sigma_{Estat}/E$) and the spatial axial resolution $\sigma_z$ are plotted in Figs. 20 and 21, again as function of the emission point $z$. For the $LaBr_3$ crystals the simulations predict excellent values in both respects. An energy resolution acc. to eq. 3 of about 6-6.5% (FWHM) seems to be achievable. The axial spatial resolution $\sigma_z$ is of the order 2 mm (150 mm) and 3 mm (250 mm long crystals), predicting an axial resolution of the positron annihilation point of 3.3 and 5 mm (FWHM), respectively. The statistical term of the LSO energy resolution is somewhat worse, however still matches the intrinsic resolution. The axial spatial resolution is also inferior compared to $LaBr_3$.

### 3.5. Spatial reconstruction resolution – Comparison with a conventional radial PET geometry

Basic M.C simulations have been performed to assess the achievable reconstruction resolution. We compare the spatial (volumetric) reconstruction resolution of the proposed axial concept with published HRRT data and simulation results of a classic (HRRT-like) radial scintillator arrangement.

For a simple and clear interpretation of the results, the simulations only consider photoelec-

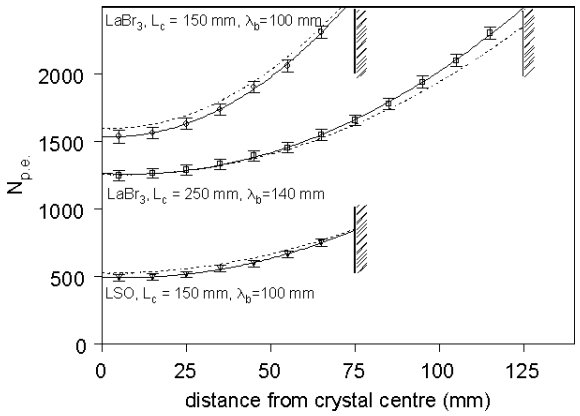


Figure 19. Variation of the detected number of photoelectrons ($E_\gamma$ = 511 keV) with the detection point along the crystal z-axis. Note that in Figs. 19 to 21 the distance is measured from the crystal centre and not from the crystal end.

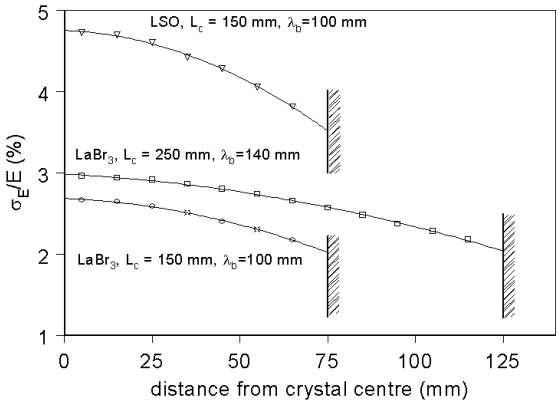


Figure 20. Dependence of the single gamma energy resolution (only statistic term, $E_\gamma$ = 511 keV) on the z-coordinate.

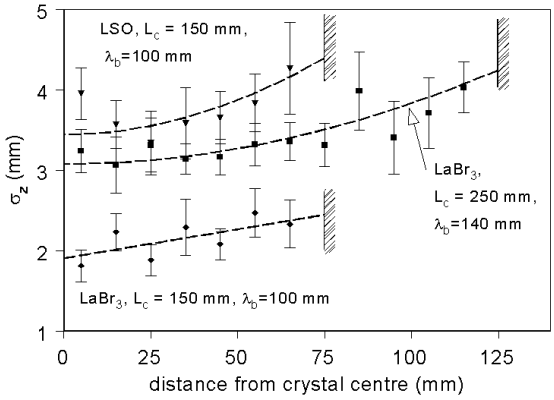


Figure 21. Dependence of the axial spatial resolution (single photons, $E_\gamma$ = 511 keV) on the z-coordinate. The dashed lines correspond to the analytical formula (eq. 9 multiplied by an empirical factor 1.13. The correction factor is required to account for the pathlength fluctuations which are not included in the analytical expression.

tric interactions of 511 keV photons disregarding Compton scatterings in the organic tissue and in the scintillator matrices. The contribution of the scatter events to the HRRT performance is difficult to be interpreted because of the lack of detailed information on the data processing from the readout of the phoswich layers. However, as it will be shown, even in these conditions, the comparison between the simulations and the published HRRT experimental data allows a good understanding of the responses.

The M.C. code starts off with a pattern of small $1 \times 1 \times 1$ mm$^3$, i.e. quasi point–like, positron sources. The range of the positrons in the organic tissue (a Gaussian distribution of 0.5 mm (FWHM) for the $^{18}F$ radiotracer) and the non-collinearity of the 511 keV annihilation photons ($180 \pm 0.25°$) are accounted for. Both the path of the positron and the emission direction of the annihilation photons follow an isotropic distribution. A scanner based on the axial geometry with a free inner diameter of 320 mm was simulated using crystals of $3.2 \times 3.2$mm$^2$ width and 150 mm (LSO) and 250 mm ($LaBr_3$) length. For the z-resolution the crystals were assumed to have a bulk light attenuation length of 100 mm and 140 mm, respectively.

The scanner based on a radial geometry consists of a circular ($\emptyset_{int.} = 46.8$ cm) arrangement of LSO crystals of $2.1 \times 2.1 \times 30$ mm$^3$ size. This geometry differs of the octagonal shape of the HRRT but should not alter too much the interpretation of the results. The photon conversion point in a hit crystal is assumed at half the crystal length.

The trajectories of the annihilation photons are extrapolated from the source to the sensitive volume. The detection points are determined according to the attenuation length and the segmentation of the sensitive volume. The line of record (LoR) is then drawn between the two detection points.

To avoid the complication of a real tomographic reconstruction, the resolution is obtained by calculating analytically the shortest distance between the line of record and the original positron emission point. The projections of this distance in the x–y (transaxial) and z (axial) direction are accumulated in histograms and fitted by Gaussian curves. Their width corresponds to the resolution searched for.

An empirical multiplication factor of 1.25 [48] is applied to the results in the transaxial plane to account for the additional uncertainty which the tomographic reconstruction procedure would introduce. As the proposed axial geometry uses individual crystal readout, a block decoding scheme (Anger logic), which would lead to further resolution degradation ($\approx$ 2.2mm (FWHM) added in quadrature [48]), is not necessary.

Small sources of $1 \times 1 \times 1$ mm$^3$ were simulated at coordinates equidistantly distributed ($x_i, y_i = 0, 2, 4, 6, 8, 10$ cm) over the transverse FOV. Figures 22 and 23 show examples of the original and reconstructed distributions in the transaxial plane for z=0.

Figures 25 and 26 show the results of the simulations with the published data of the HRRT [12,13], see also Table 2. The resolutions are derived from Gaussian fits to the distributions of the x-y - in the transaxial plane – and z projections of the shortest calculated distance between the reconstructed LOR and the true positron annihilation point.

For illustration purposes the same source configuration has been simulated and reconstructed for a HRRT-like radial geometry with crystals of 30 mm length (see Fig. 24). At 10 cm from the centre of the FOV, and without DOI measurement (Phoswich technique not employed), the parallax error in the transaxial plane is sizable and gives rise to a clear astigmatism.

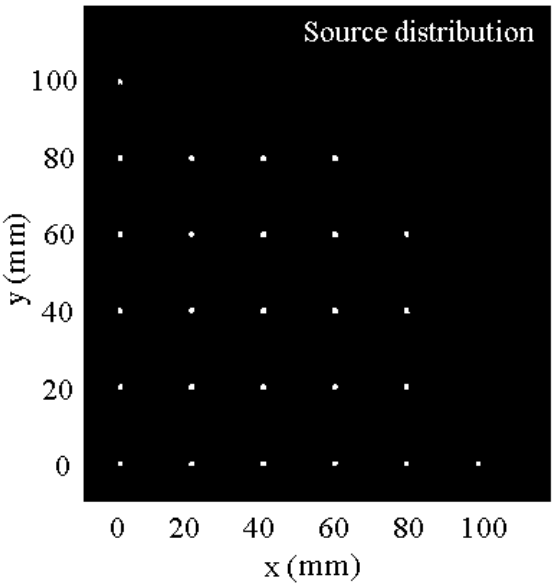


Figure 22. Distribution of the pointlike sources ($1 \times 1 \times 1$ mm$^3$) in the transaxial (x–y) plane at z=0.

The comparison of the HRRT experimental resolutions with the simulations is more difficult to analyze in absence of detailed informations on the data processing. In the transaxial plane, at centre of the FOV there is a difference of about 35% between the data and the simulations which can be explained by the contribution of Compton interactions in the scintillator blocks. At 10 cm off centre, the agreement is good because the dominant contribution to the resolution is the parallax error well accounted by the simulation. For the axial z coordinate, the conclusion of the comparison is inverted. At centre of the FOV the agreement is good within the errors. At

Table 2
Comparison of reconstruction resolution (FWHM values): HRRT data vs. HPD–PET simulation. In the simulations a crystal length of 150 mm was assumed. All values correspond to the central plane (z=0).

| | Transaxial resolution $R_x(= R_y)$ (mm) | | Axial resolution $R_z$ (mm) | | Mean volumetric resolution $R_V = R_x \times R_y \times R_z$ (mm$^3$) |
|---|---|---|---|---|---|
| | x=0; y=0 | x=100; y=0 | x=0; y=0 | x=100; y=0 | |
| HRRT data, span 9 | 2.35 | 2.75 | 2.5 | 3.6 | 20 |
| HRRT data, span 3 | 2.35 | 2.75 | 2.5 | 2.8 | 18 |
| HPD-PET LSO | 1.85 | 2.35 | 5.78 | 6.33 | 26 |
| HPD-PET $LaBr_3$ | 1.59 | 2.13 | 3.43 | 3.57 | 11.8 |

10 cm off centre the deviation strongly depends on the esoteric axial data compression, characterized by span and ring difference which determine the maximum angular acceptance.

As the Compton events are clearly reconstructed with the axial PET concept, one must compare the M.C simulations with the experimental data of the HRRT. At centre of the FOV ($x = 0$), the resolution has the expected value, independently of the crystal choice, but degrades by about 40% at $x = 10$ cm because of the asymmetry of the LOR with respect of the emission point. As previously stressed, the high photon yield of $LaBr_3$ crystals significantly improves the axial resolution.

With 15 cm long $LaBr_3$ crystals a mean volumetric reconstruction resolution of 11.8 mm$^3$ is attainable, hence about 40% better than the HRRT measured one. For 15 cm long LSO crystals the expected resolution is about 14% worse than the HRRT results. This last performance would obviously improve by a factor 0.86 if LSO would be replaced by LYSO crystals with a photon yield of 35 ph/keV in addition by a factor 0.85 by increasing the photocathode quantum efficiency from 18 to 25%.

## 4. Detection efficiency for *true* PET events

In this paragraph we discuss, from a physics point of view, the detection efficiency of True (T) events for photon incidence normal to the scintillator array. The values thus obtained are characteristic of the matrix configuration and of the scintillating material, independently of the scanner geometry.

A True event is defined as the detection of two annihilation quanta of 511 keV energy emitted in opposite directions and which undergo either a photoelectric conversion or a Compton scattering in the matrix of scintillators which, unambiguously, can be reconstructed.

The results which are given in table 3 are derived from analytic calculations and suffer of inevitable approximations. Their validity, however, was tested for a matrix of LSO crystals with a M.C simulation using GEANT 4 code. Agreement was found within about +-10% error. The detection efficiencies are rather underestimated, but allow a coherent comparison of the expected performances with those of the HRRT-PET scanner.

The values of photon cross-sections, attenuation and absorption lengths for 511 keV photons are listed in table 1, and were derived by interpolation from the Hubbel tables of the National Bureau of Standards.

### 4.1. Compton scattering : Reconstruction and limitations

In order to unambiguously distinguish the coordinates of the primary Compton interaction of those of the secondary interactions (photoelectric conversion or Compton scattering) the reconstruction program restricted to events in which the photon of the primary Compton scattering is

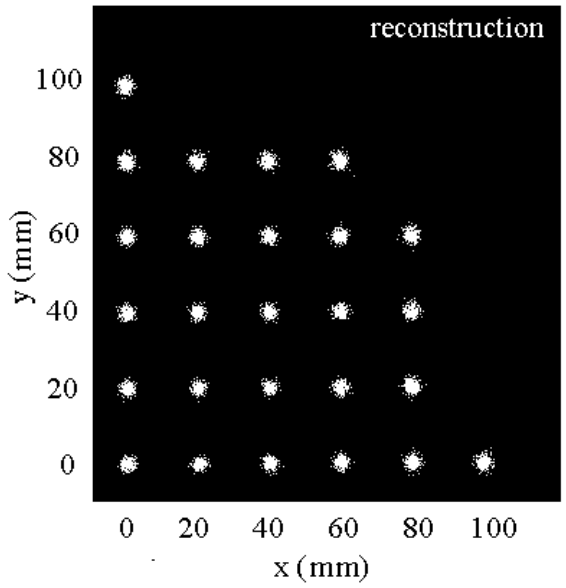


Figure 23. Reconstruction of the source distribution in the transaxial (x–y) plane at z=0.

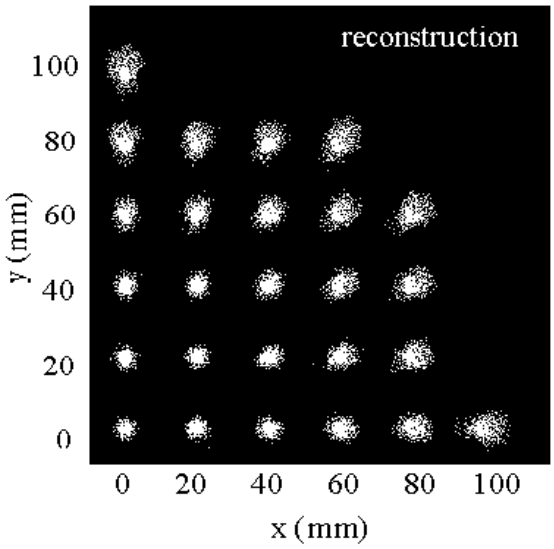


Figure 24. As Fig. 23, however for a radial arrangement of 30 mm long crystal.

emitted in the forward direction.

We have used as selection criteria, the Klein-Nishima formulation which describes the kinematics and the cross section dependence with the incident photon energy and scattering angle $\theta_C$ (see Figs. 27 and 28).

A detailed analysis shows that the scattering angle in the forward hemisphere must be restricted to $0 < \theta_C < 60°$ if the energy of the recoil electron in the primary interaction is below 170 keV for 511 keV photons. About 60% of all scatter events fall in this category. However, for reconstructing with an acceptable precision the z axial coordinate a minimum recoil electron energy of 50 keV is required, a limit which conceptually is not needed for the reconstruction in the transaxial plane. Finally, the acceptance in energy between 340 and 460 keV of the scattered photon reduces to about 25% the fraction of scatter events which unambiguously can be reconstructed.

### 4.2. Estimation of the detection efficiency

If $\lambda_{att}$ is the attenuation length of incident 511 keV photons, the probability of interaction in a scintillator of thickness $t$ is $1 - \exp(-t/\lambda_{att})$ and the mean depth of interaction $\langle DOI \rangle = \lambda_{att} - t/(\exp(t/\lambda_{att}) - 1)$. Therefore, the residual mean path for a photon emitted in the forward direction is simply $\langle t_{res} \rangle = [t/(1 - \exp(-t/\lambda_{att}) - \lambda_{att}]/cos(\theta_C)$. Hence the probability of a $2^{nd}$ interaction (photoelectric or Compton int.) in $\langle t_{res} \rangle$ is $1 - \exp(-\langle t_{res} \rangle/\lambda_{att}(E_C))$, and the probility of a full absorption $1 - \exp(-\langle t_{res} \rangle/\lambda_{abs}(E_C))$.

The results shown in Table 3 have been obtained assuming a mean photon energy in the primary Compton interaction of 400 keV.

In Table 3 two selection criteria of unambiguously reconstructed Compton events are given. For the first criteria a scatter event is selected as T if the scattered photon undergoes a secondary photoelectric conversion, whilst for the second criteria an event is taken as T if the total energy is lost in the scintillator matrix.

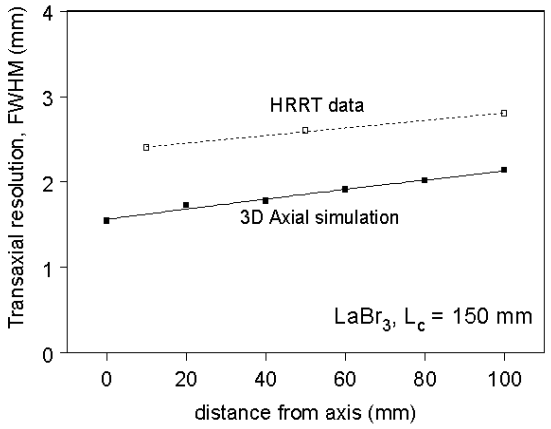


Figure 25. Resolution of spatial reconstruction in the transaxial (x–y) plane. The simulation results are for $LaBr_3$ crystals of 150 mm length. The HRRT data has been extracted from ref. [12].

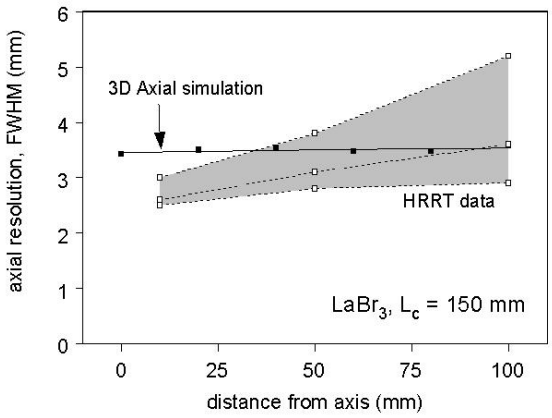


Figure 26. Resolution of spatial reconstruction in the axial (z) plane. The simulation results are again for $LaBr_3$ crystals of 150 mm length. The grey shaded area corresponds to HRRT data (ref.[12]) obtained in different operation and reconstruction modes.

A sensitivity of 4.4 cps/kBq has been measured for the HRRT [10] with a phantom of 20 cm in diameter and 20 cm in length, in conformity with the standard NEMA-NU2 test protocol. However, according to M.C simulations of the HRRT (see next par.) one expects a sensitivity of 2.9 cps/kBq for the detection of two coincident photons that underwent a photoelectric effect. The difference can be understood by the detection of Compton scattered events which develop in a single scintillator block and, for part, are not rejected by their detection in both phoswich layers. This scatter events enhance the detection efficiency for two coincident annihilation photons from 4.6 to 6.9% (see table 3).

Note that for the axial PET-HPD we assume a total scintillator thickness of 41.2 mm for LSO crystal bars, hence 13 layers of 3.2 mm according to the design discussed in sect. 2.1, and 51.2 mm ($16 \times 3.2$ mm) for $LaBr_3$ coresponding to a 90° rotation of the previous matrix configuration.

Using LSO (LYSO) scintillators the intrinsic detection efficiency of the PET-HPD matrix is a factor about 2.5 higher than the one of the HRRT.

Because the photofraction of $LaBr_3$ is a factor twice lower than the one of LSO the Compton enhancement is dominant but, as it can be seen, the detection efficiency is lower. As the attenuation length of $LaBr_3$ crystal is long compared to LSO, their use requires a larger matrix volume hence a significant increase of the cost.

### 4.3. PET sensitivity and NEMA-NU2 protocol of characterization

The sensitivity, i.e. the True event rate T per activity (cps/kBq), and the scatter fraction ($SF = S/(S+T)$) have been estimated in the conditions of the NEMA-NU2 test protocol using a phantom of 20 cm in diameter et 20 cm long filled with a dilution of $^{18}F$ in water. $S$ denotes the event rate involving photons which underwent Compton scattering in the patient (or phantom).

If concentrations up to 1 or 1.5 $\mu$Ci/ml are usually used to measure the dependence of the Noise Equivalent Count rate $NEC = T^2/(T+S+R)$ with the electronic dead time, we assume for the present estimates a low radioactivity. Here $R$ describes the rate of random coincideces.

M.C simulations of the NEMA experimental

Table 3
Comparison of detection efficiencies: HRRT vs. PET-HPD (at normal incidence)

| | **LSO:Ce** | | **$LaBr_3$:Ce** | |
|---|---|---|---|---|
| detector | HRRT | 3D Axial | 3D Axial | - |
| detector depth | 15 mm | 41.2 mm | 51.2 mm | $\infty$ |
| **single photon efficiencies** | | | | |
| a) photoelectric | 21.4% | 30% | 13.8% | 15% |
| b) C $\rightarrow$ pe | 4.8% | 5.7% | 3.4% | |
| c) C $\rightarrow$ C $\rightarrow$ pe | 4.8% | 4% | 2.6% | |
| d) C $\rightarrow$ absorption | | 12.6% | 12.3% | $\sim$ 21% |
| i) a+b+c | 26.2% | 39.7% | 19.8% | |
| ii) a+d $\rightarrow$ absorption | | 42.6% | 26.1% | $\sim$36% |
| **photon pair efficiencies** | | | | |
| i) a+b+c | 6.9%[1)] | 15.7% | 3.9% | |
| ii) a+d | | 18.1% | 6.8% | $\sim$ 13% |
| ratio HPD-PET / HRRT | | | | |
| i) a+b+c | | 2.3 | 0.6 | |
| ii) a+d | | 2.6 | 1 | |
| Compton enhancement | | $\sim$2.0 | $\sim$2.5 | |

[1)] HRRT data. For pure photoelectric events a photon pair efficiency of 4.6% would be expected. We conclude that the HRRT events contain a substantial fraction of events with Compton interactions.

test configuration have been performed for the PET-HPD and the HRRT scanners to determine the respective solid angle for detection of T events. The mean value of the acceptance ($\Delta\Omega/4\pi$) thus estimated is 0.165 for the axial PET design with 150 mm long crystals and 0.344 for the HRRT respectively.

The photon mean free path calculated from the distribution of the path lengths inside the phantom for detected photons is 8.55 cm. Therefore, for a photon attenuation length of 10.3 cm in water ($\mu_{att}$(511 keV)= 0.097cm$^{-1}$) the probability of a True event to escape the phantom is $\exp(-17.1/10.3) = 0.19$.

Taking the detection efficiencies listed in table 3 one can estimate a PET-HPD sensitivity of 2.7 and 5.5 cps/kBq without and with Compton enhancement respectively.

For the HRRT, as already quoted, a sensitivity of 4.4 cps/kBq is estimated from a measurement of $S + T$ events, by assuming according to the authors a $SF$ of 0.4, which suggests the detection of Compton events but with a limited degradation of the spatial resolution.

## 5. Figure of merit: Estimate and comparison

We define a figure of merit as,

$$FoM = \epsilon_{det} \cdot \frac{\Delta\Omega}{4\pi} \cdot QF \tag{10}$$

where $\epsilon_{det}$ is the detection efficiency for $T$ events and $\Delta\Omega/4\pi$ describes the acceptance of the scanner. We introduce the quality factor $QF = (\frac{\Delta E}{E} \cdot R_V)^{-1}$ as a combination of energy and spatial resolution, which to a certain extent characterizes the achievable image contrast. The quantity $FoM$ can therefore serve for a global characterization of the *overall technical performance*. The impact of the running conditions on the image contrast through the detection of scatter events ($S$) in the organic tissues and of random coincidences ($R$) is obviously ignored in this simple approach. While the $S$ rate depends on the discrimination in energy of the detected photons, the $R$ rate is determined by the width of the coincidence time window. This aspect is discussed in the next section devoted to data acquisition (DAQ) system.

Table 4
Performance summary and comparison

| | **HRRT** | **PET–HPD** | | | | | |
|---|---|---|---|---|---|---|---|
| scintillator | LSO:Ce | LSO:Ce | | | $LaBr_3$:Ce | | |
| AFOV (mm) | 250 | 150 | | | 150 | | |
| detector depth (mm) | 15 | 41.2 (13 × 3.2) | | | 51.2 (16 × 3.2) | | |
| $\Delta\Omega/4\pi$ | 0.344 | 0.165 | | | 0.165 | | |
| | measured | PE | Compton | total | PE | Compton | total |
| $\epsilon_{det}(2\ photons)$ (%) | 6.9 | 8.5 | 7.2 | 15.7; 18.1 | 1.9 | 4.9 | 6.8 |
| $\Delta E/E$ (511 keV) (%) | 17 | 10.3(z=0), 12.4(z=L/2) | | | 4.7(z=0), 5.3(z=L/2) | | |
| $\Delta V$ ($mm^3$) | 20 | 22 | ∼45 | ∼33 | 11 | ∼22 | ∼18 |
| $\Delta E/E \cdot \Delta V$ (%·$mm^3$) | 340 | 250 | ∼510 | ∼370 | 55 | ∼110 | ∼90 |
| $FoM$[1)] | 0.7 | 0.6 | 0.25 | 0.8 | 0.6 | 0.74 | 1.25 |
| Compton enhancement | | | | 1.85 | | | 2.8 |
| sensitivity (cps/kBq) | 4.4 | 2.7 | 2.8 | 5.5 | 0.6 | 1.0 | 2.1 |

[1)] Figure of Merit $FoM = \epsilon_{det}(2photons) \cdot \frac{\Delta\Omega}{4\pi} \cdot (\frac{\Delta E}{E} \cdot R_V)^{-1}$ ($mm^{-3}$)

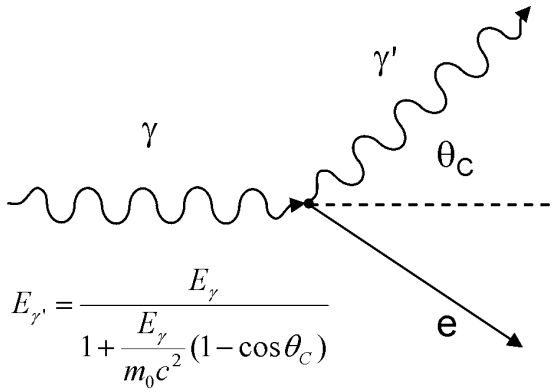


Figure 27. Kinematics of the Compton interaction.

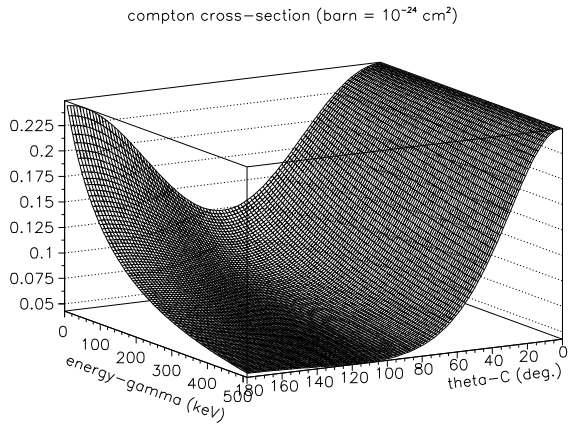


Figure 28. Cross-section for Compton interaction as function of scattering angle $\sigma_C$ and photon energy.

The comparative results are shown in Table 4.

Because of the low recoil electron energy, the axial resolution of the reconstructed Compton events degrades, worsening the spatial resolution DV. However, despite an acceptance a factor 2 lower than the HRRT, the merit factor of the PET-HPD with LSO scintillators is comparable but it is about 70% higher with $LaBr_3$.

It must be noticed that the quality factor $QF$ varies roughly proportionally to the number of detected photoelectrons. Therefore, if a light yield of $35 \cdot 10^3$ photons/MeV (LYSO) is attainable and by improving the photocathode quantum efficiency at 420 nm from 18 to 25% (standard commercial value), the figure of merit of the discussed 3D Axial PET could be two times larger than the one of the HRRT. A design with 25 cm long $LaBr_3$ crystal bars does not allow an improvement of the

figure of merit despite the increase of the acceptance because of the spatial and energy resolution degradation.

The intrinsic $FoM$ is, obviously, affected by the performances of the FE electronic and the DAQ system which determine the image contrast $T/(T + S + R)$ as a function of the operating environment (radioactivity).

## 6. Data acquisition

### 6.1. Principle and limitations

The principle of the data acquisition (DAQ) system and its particular features are driven by two main constraints: (i) the readout architecture of the VATA front-end chip and (ii) the requirement to detect and analyze photon interactions, which involve Compton scattering in the detector.

The tracking of the latter interactions requires to run the FE electronic with a relatively low detection threshold of about 50 keV/channel in order to detect and reconstruct the recoil electron of the primary Compton scattering. However, the low threshold prevents the rejection of a large fraction of photons which underwent Compton scattering in the organic tissue. Such discrimination is used in all conventional PET systems, as it allows to drastically decrease the counting rate and thus also reduces the rate of accidental coincidences.

In the so-called *sparse readout mode*, the VATA readout sequence consists of a multiplexed sequential readout of only those channels with a hit (see Sect. 2.4). The front-end chip can be operated at a clock speed of 20 MHz. This leads to a mean readout time of $\approx 1.2\mu$s per event, depending somewhat on the selection criteria applied to the hit multiplicity. Without a stringent selection of events, the electronic dead time would paralyze the readout system already for modest source activity levels and hence spoil the sensitivity of the PET scanner.

It is a unique and intrinsic property of the HPD photodetector which allows to resolve this problem. The HPD provides a fast measurement of the total energy deposited in the scintillator matrix. The total energy information is derived from the induced signal on the Si sensor back plane which, as it covers the full detector area, is proportional to the total amount of charge deposited in the Si sensor, and hence to the total energy converted in the scintillator block. As will be detailed below, the large and prompt back plane signal allows to identify and reject low energy photons (from Compton scattering in the patient), without compromising the ability of the FE electronic to detect Compton interactions in the scintillator matrix. This is an essential and fundamental feature of our approach and the proposed DAQ concept.

To better understand the limitations of the DAQ, Table 5 shows the dependence of the trigger rates with various event selection criteria, like energy threshold for the generation of a Fast OR ($FOR$ signal) and multiplicity of crystal clusters. The numbers were estimated in the conditions of the NEMA-NU2 test protocol from M.C simulations and analytic calculations, within $\pm 10\%$ error. The rate of accidentals was estimated on the basis of a Coincidence Time Window (CTW) of 10 ns for a phantom radio-tracer concentration of $0.35\mu$Ci/ml ($V = 6310$ ml, i.e. total activity = 81.4 MBq).

Operating the FE electronic with a detection threshold of 50 keV without additional event selection would require a huge and technically unfeasible DAQ rate. The conditions improve significantly when applying a cut-off on the hit multiplicity and, obviously, drastically, if the detection threshold is raised to 400 keV (right most column in Table 5), a value which greatly favors the detection of unscattered photons of 511 keV.

Running with a detection threshold of 50 keV, which enables *Compton sensitivity enhancement*, and exploiting at the same time the total energy information from the Si sensor back plane, leads to a reduction of the DAQ rate by a factor of about 14. However, even in these conditions, a reasonably achievable DAQ rate of 0.5 to 0.6 MHz would result in a poor acquisition efficiency of about 50%. Therefore, as described below, the DAQ system is split in several parallel and independent chains. In the following we discuss a 3D Axial PET scanner comprising 16 modules.

Note that for an activity of 81.4 MBq the count rate of the $FOR$ signal is of the order 1.9

Table 5
Trigger selection criteria and DAQ rates

| Si sensor back plane readout | | no | | | yes, $E_\gamma \geq$ 400 keV |
|---|---|---|---|---|---|
| energy threshold $FOR$ | | 50 keV | 50 keV | 400 keV | 50 keV |
| selection: hit multiplicity | | any | $m \leq 2$ | $m = 1$ (photopeak) | any |
| phantom activity | interaction type | **relative count rate (cps/kBq)** | | | |
| low[1)] | single $\gamma$ (PE + Compton) | 280 | 115 | 49 | 280 |
| low | 2 coincident $\gamma$s (PE + Compton) | 90 | $\sim 18$ | $\leq 3$ | 90 |
| low | DAQ rate | 90 | | | 6-7 |
| | | **absolute count rate (cps = Hz)** | | | |
| 81.4 MBq[2)] | DAQ rate (8 parallel DAQ chains) | $7.3 \cdot 10^6$ Hz | | | $5 - 6 \cdot 10^5$ Hz |
| 81.4 MBq | accidental's rate (CTW = 10 ns) | $\sim 1.2 \cdot 10^6$ Hz | | | $\sim 10^5$ Hz |

[1)] Random count rate is negligible. [2)] 81.4 MBq = 0.35 $\mu$Ci/ml $\times$ 6310 ml.

MHz/module but decreases to 0.7 MHz/module for a threshold setting of 50 keV.

For $N_m = 16$ modules covering the azimuthal acceptance, there are $N_m \cdot (N_m - 1)/2 = 120$ possibilities to form module pairs. From the geometrical point of view, only roughly half of them will lead to physically meaningful coincidences ($T$ and $S$ events), but all of them will contribute to the random rate ($R$). To minimize these accidentals the DAQ architecture is designed to accept coincidences of hit modules only within a limited angular acceptance, e.g. five or six modules in the opposite hemisphere (see Fig. 29). The DAQ system thus searches for coincidences between a given module and, for example, the 5 or 6 opposite modules. This reduces the number of valid module combinations and consequently the associated accidentals rate by more than a factor 2.

This *selective pair approach* allows to structure the DAQ architecture as 8 coincidence chains, which are defined dynamically and work in parallel in an independent and asynchronous way. A coincidence chain consists of a first module and a dynamically associated second module from the opposite hemisphere. When a chain detects two module pairs in coincidence, all other modules are unaffected and stay armed for other coincidences.

The detection of randoms $R$ is strongly suppressed w.r.t. $T$ and $S$ events by requiring coincidences of exactly two modules. The randoms rate due to uncorrelated single photons simulating $T$ events decreases by a factor of about ten after energy discrimination, but still constitutes about 20% of the acquired data. The estimated image contrast $T/(T + S + R)$ is about 0.6, compared to 0.4 for the HRRT.

### 6.2. Energy discrimination

The signal charge, produced in the HPD ($U_C$ = 12 kV), following the absorption of a 511 keV photon in a LSO crystals, ranges from 0.87 to $1.23 \cdot 10^6$ electrons (0.14 - 0.2 pC), depending on the axial coordinate at which the crystal bar is hit. The induced signal on the back plane of the sensor is almost fully due to the holes drifting over the full thickness of the Si sensor (300 $\mu$m). The pathlength of the electrons (few $\mu$m) does not give a sizable contribution. Operating the sensor above the full depletion voltage ('overbias'), $U_{bias} \sim 3 \cdot U_{dep}$, the $\sim 10^6$ holes will induce a current of about 10 $\mu$A during the total drift time of less than 15 ns. A low impedance and large band-

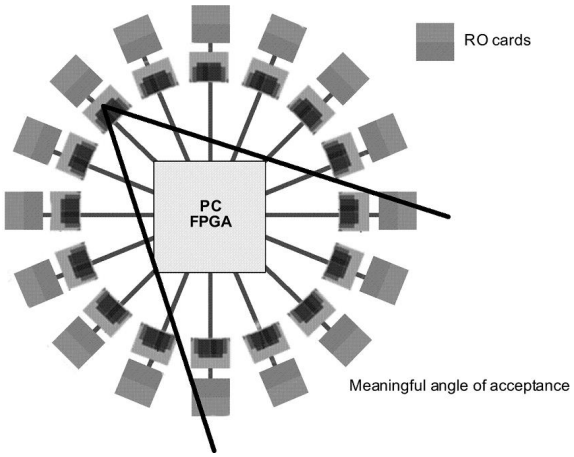


Figure 29. Schematic representation of the 16 readout modules. For each of the modules a geometrical acceptance range is defined in which coincidences with other modules can be formed.

width amplifier (70 MHz) with a shaping time of 5 ns will be able to sense about 1/3 of the total charge, i.e. about $3 \cdot 10^5 e^-$. Such an amplifier has a typical noise of about $2 \cdot 10^3 e^-$ (RMS) even though the backplane capacitance is about 300 pF. This means that the back plane signal can be detected with a very comfortable signal to noise ratio of about 150.

The signal from the back plane of the silicon sensor is proportional to the total energy deposited in the crystal matrix. Therefore, it does not differentiate between a photoelectric interaction, where usually only one crystal bar is affected, and a detection sequence involving a Compton interaction, where generally several crystal bars are affected.

Summing just the analogue signals $A_L$ and $A_R$ of the left and right HPD does not provide an accurate energy discrimination. Due to the light absorption in the crystals, the sum $A = A_L + A_R$ varies for the same energy deposit from 0.28 to 0.4 pC for interactions occurring at the centre and at the bar end, preventing the application of a precise cut for energy discrimination of $S$ events. A threshold setting equivalent to 400 keV at the centre, for example, would correspond to a discrimination threshold of 310 keV at the bar end. By using instead the variable $(A_L + A_R) - 0.5 \cdot |A_L - A_R|$ reduces the maximum dispersion by more than a factor two allowing a threshold of $419 \pm 22$ keV.

The fast response of the sensor back plane is obviously exploited, as described below, for the search of coincidences between modules allowing a time resolution of 5 to 10 ns.

### 6.3. DAQ architecture

To minimize the DAQ related dead time, only the module pair detected in coincidence during the $CTW$ is read out, while all other modules remain enabled to accept further coincidences. The system is thus continuously running: some modules can be in the readout state while others are awaiting coincidences.

This implies that the DAQ architecture foresees one readout card per module, which deals with four VATA chips (two chips per HPD). With this configuration the DAQ system can read out the 16 modules (or potentially more) independently in parallel. All the 16 cards are controlled by a single Process Controller ($PC$) – implemented as Field Programmable Gate Array (FPGA) – that checks for the pair of modules in coincidences and enables their readout (see Figs.30 and 31).

The $PC$ receives all the flag signals ($FORM$) from the discriminator of the analogue signal $A$ of each module, and performs, when a coincidence is detected in the $CTW$, the combinatorial selection of meaningful Line Of Records (LOR).

When a module is not in a readout sequence, the VATA chips run in a self reset operation mode: the $FOR$ output of each chip is applied to its reset input after a *reset delay* of 25 to 30 ns. This delay is driven by the performance of the time walk compensation circuit, when fed with signals of different amplitudes (see sect. 2.4 ).

If on the contrary a coincidence is detected, the PC blocks the $RESET$ signal and inhibits teh VATA chip after a dealy of 50 to 90 ns with respect to the occurence of true event. The inhibition, i.e. the vetoing of undesired data in the VATA output registers, is performed by setting the *Discard Late Trigger* (DLT) Signal of the

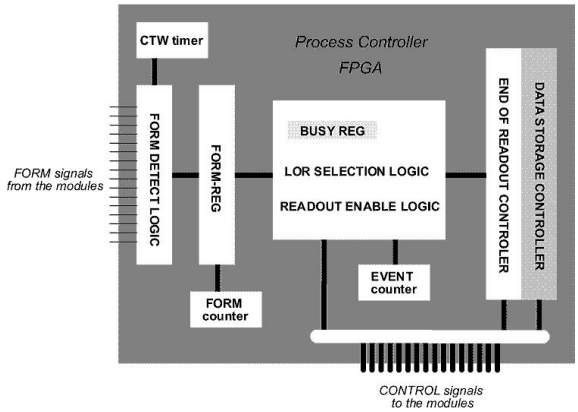


Figure 30. Components and functionality of the Process Controller.

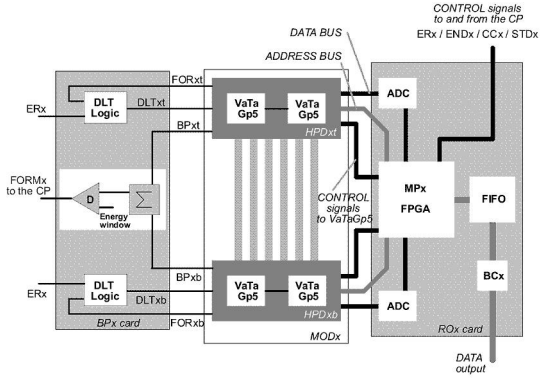


Figure 31. Schematic representation of the signal and data flow. The central box represents a detector module with 2 HPDs.

VATA chip.

In these operational conditions the rate of random coincidences for a radiotracer concentration of 0.35 microCi/ml is only 4.2% for a time resolution of 5 ns if 6 opposite modules are eligible for coincidences. The probability of two events piling up in the VATA output registers within the *reset delay* (30 ns) is of the same order. However these pile-up events can be rejected by the offline analysis and only degrade the DAQ efficiency without spoling the data quality. The electronic dead time is thus mainly determined by the readout time sequence of the VATAs as discussed below.

The DAQ sequence is as follows:

When the Process Controller has detected a coincidence in the $CTW$ acceptance the $FORM$s are stored in a register ($FOR_M$), counted and a busy flag ($BUSY_M$) is generated after a delay of 50 ns. The $BUSY_M$ signal disables the self reset of the VATAs of all hit modules, and 40 ns later inhibits the chip operation.

If the $FOR_M$ counter shows two photons in coincidence, the Process Controller keeps high the $BUSY_M$ on the DLT input of the two hit modules and increases the value of an event counter ($EC$). If, however, the $FOR_M$ counter shows less (no coincidence) or more than 2 (accidental hits), the $PC$ enables the VATA chips of the hit modules ($BUSY_M$ low) and resets their registers and busy flags.

As an option, the Process Controller can still check the multiplicity of hit crystal bars per module, which gives a good indication whether the photon was detected by photoelectric effect or a more complex interaction sequence involving Compton scattering. For this purpose the VATA chip provides a fast analog signal which is proportional to the hit channel multiplicity. After discrimination, a flag ($REG_{mul}$) can be generated. This step ends the first part of the processing.

Assuming a veto time of 12 ns for each generated $FOR$ of the 8 top modules $TM_i$ which start the search for coincidences, the time fraction during which the FE electronic will be vetoed for a radioactivity of 0.35$\mu$Ci/ml (or 1.9 Mhz counting rate per module) is about $1.9 \cdot 10^6 \times 12 \cdot 10^{-9} = 0.023$. This leads to selection efficiency of $\epsilon_{sel} = exp(-0.182) \sim 98\%$, considering only this first part of the acquisition process.

In case of a *good event*, i.e. if all the above described criteria are met, the Process Controller enables the Module Controllers $MC$ (also implemented as FPGA's) of the hit modules to read and save:

**(i)** the value of the event counter ($EC$) in the registers of the $MC$ (header of the event

buffer)

**(ii)** the addresses of the hit modules in coincidence registers $CR$.

As soon as they receive the $ENABLE$ signal from the Process Controller, after a delay corresponding to the peaking time $\tau_s$ of the shaper in the analogue chain of the VATA-GP5 the $MC$'s send the $HOLD$ signal to the corresponding modules. Then the $MC$'s start to readout and encode the data using the sparse readout mode of the VATA chips. ADCs with 12 bit resolution are well suited to the dynamic range. The $MC$ verify for each read module that the hit channels and the multiplicity of the two HPDs correspond. In case of LSO crystals a mean value of 3 hit channels is expected. With a clock frequency of 20 Mhz, the mean readout time per module is $(3+3) \times 50 \cdot 10^{-9}$ s $= 0.3\mu$s (3 initial clock cycles are needed to address the first data). For a total readout rate in the 500 kHz range, shared between the 8 DAQ chains, and a radiotracer concentration of $0.35\mu$Ci/ml, we estimate a busy fraction of the system of $500 \cdot 10^3$ s$^{-1}$ $/8 \times 0.3 \cdot 10^{-6}$ s $= 0.019$, resulting in a *readout efficiency* of $\epsilon_{RO} = \exp(-0.019) \approx 98\%$. The total efficiency of the DAQ system is hence $\epsilon_{DAQ} = \epsilon_{sel} \cdot \epsilon_{RO}$ =96%.

After acquisition, the data (addresses of the hit modules and the digitized signal amplitudes) are stored in a local FIFO memory present in each $MC$. Asynchronous data transfer to the computer (standard personal computer) is implemented via a fast suitable network protocol. In the prototype phase USB 2.0 is planned to be used which provides a bandwidth of 3.75 MHz per module. For the full implementation a 10 Gbit optical fiber link is a more appropriate option.

## 7. Conclusions

We described the innovative geometrical concept and a possible implementation of a 3D Axial PET scanner and its dedicated data acquisition system. The performance estimates for the reconstruction resolution in both the axial and transaxial plane and the uniformity of the resolution over the complete field of view make the concept very competitive in comparison with existing state-of-the-art devices. The possibility to unambiguously reconstruct part of annihilation photons which underwent Compton scattering in the crystal matrix is a unique feature of the concept and leads to high sensitivity even for limited solid angle coverage. The use of recently developed fast high-Z and high density crystals like $LaBr_3$ leads to excellent energy resolution, which is expected to facilitate scatter suppression and consequently will boost image contrast.

The described study is currently still on a conceptual level. Several findings require support by more elaborated and comprehensive simulations, which need to take into account effects linked to tomographic data reconstruction. A major milestone, the proof of principle in form of a 3D Axial camera protoype module, is under preparation. Most of the required hardware components have been developed and are now available. We will report about the experimental results in a forthcoming paper.

## Appendix

### Experimental determination of the light absorption length

The determination of the axial z coordinate of the photon conversion point is affected by an error $\Delta z$ that strongly depends on the precision with which the effective light absorption length $\lambda$ for the light emitted in the crystal bar, is known. As shown by the equations 8 and 9, in order to achieve the required precision of 1 mm in z, one must measure $\lambda$ with a precision $\Delta\lambda/\lambda$ better than 1.3% and 0.8% for crystals of length L of 150 and 250 mm, respectively. The experimental method used to evaluate $\lambda$ consists in measuring the ratio between the pulse heights $Q_R$, $Q_L$ recorded at both ends of the bar as a function of the axial excitation position. Assuming an optically isotropic crystal, one expects a ratio $Q_R/Q_L = 1$ when the scintillation light is emitted at $L/2$, and an exponentially decreasing ratio when the emission point is displaced from one bar end ($z = 0$) to the opposite one ($z = L$). The effective attenuation length

$\lambda$ is eventually evaluated from the relationship $Q_R/Q_L = exp[(L-2z)/\lambda]$.

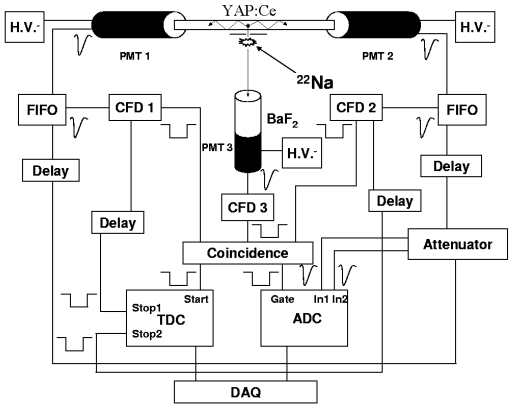


Figure 32. Schematic of the experimental set-up.

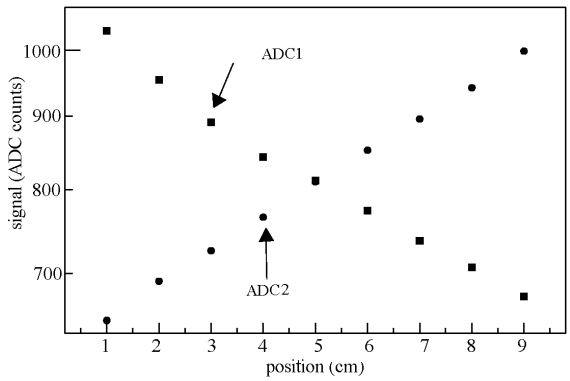


Figure 33. Signal amplitude (ADC counts) measured at the two crystal ends as a function of the axial emission position.

The schematic of the test bench used for the light absorption length measurement in shown in Fig. 32. Hamamatsu photomultipliers (PMT) H-3165-10 are coupled to each crystal bar with optical grease (BC-630[14]), with a refractive index $n = 1.47$ at 400 nm, to reduce photon losses due to the reflection at the 10 mm diameter photomultiplier window. No specific reflector material is used to wrap the crystal bars, thus scintillation light reaches the PMTs either directly or via total internal reflection from the bar lateral sides. The PMTs, operated at a negative voltage of 1300 V corresponding to a gain of $10^6$, are equipped with a standard bialkali photocathode whose quantum efficiency, peaked at about 400 nm, matches the crystal emission wavelength. The crystal is exposed to a finely collimated beam of 511 keV photons from a 10 mCi $^{22}$Na source. A linear motion stage allows to study the light emission as a function of the excitation position by moving the crystal in nine positions along its axis, with an incremental step of 1 cm. Trigger signals are provided by the coincidence between the right–left PMT signals and the signal produced by one of the two back-to-back $^{22}$Na annihilation photons into a 28 mm thick $BaF_2$ crystal. Pulse heights and timing information, digitized by means of a LeCroy 2249W charge-sensitive ADC and a CAEN C414 TDC respectively, are recorded by a multi-parametric acquisition system running under LabView. Measurements performed on 100 mm long YAP:Ce crystals [15] gave a mean value of the effective light absorption length in YAP:Ce of about 190 mm. The bulk absorption length (compare Section 3.1) $\lambda_b = \lambda/k = 190/0.7 \sim 270$ mm appears to be almost double the value reported in [49]. The overall precision of 2% on a single measurement is within expectations given for 100 mm long crystal bars. Such a long absorption length is unsuitable for the 3D axial scheme. However, studies on various reflective coatings have already demonstrated that the effective absorption length can be tuned to a suitable value (e.g. 100 mm) while the total light output and hence the energy resolution is maintained [50].

[14]Saint – Gobain Group, Bicron

[15]The crystals were purchased from Crytur LTD., Czech. Republic.

**Acknowledgements**

We would like to thank the numerous colleagues who helped in clarifying discussions to come to a better understanding of the potential and limitations of the proposed concept. Thanks to Wojtek Dulinski (LEPSI Strasbourg) for the mask design of the Silicon sensor. We acknowledge the great support of our technical personnel at CERN Francoise Cossey, Claude David, Luc Kottelat and Ian Mcgill, which was indispensable for the construction of the photodetector prototypes. We are grateful for the financial support by the CERN technology transfer service.

## REFERENCES

1. The changing design of positron imaging systems. M.E Phelps and S.R Cherry (1998) Clin. Pos. Imag. 1(31-45)
2. The merging of biology and imaging into molecular imaging. M.E Phelps (2000) J. Nucl. Med. 41(661-681)
3. Trends in PET imaging. W.W.Moses (2001) NIM A 471(209-214)
4. Positron mission tomography (PET) advances in neurological Applications. V.Sossi (2003) NIM A 510(107-115)
5. Positron emission tomography in oncology with 18F-FDG. J.N Talbot et al. (2003) NIM A 504(129-138)
6. Particle detectors for biomedical applications demand and trends. N.A Pavel (2002) NIM A 478(1-12)
7. Detector technology challenges for nuclear medecine and PET. P.K Marsden (2003) NIM A 513(1-7)
8. Resolution and sensitivity in positron emission tomography: New frontiers. V.Sossi (2003) Proceedings Como conference World Scientific, in press
9. Performance measurements for the GSO based brain PET. Camera (G-PET) S.Surti et al (2001) Proceedings IEEE Nucl. Symposium and Medical Imaging Conf. San-Diego, CA (Nov. 4-10, 2001) p.1109-1114
10. Performances results of a new DOI detector block for a High Resolution PET LSO Research Tomograph HRRT. M.Schmandt et al. (1998) IEEE Trans. Nucl. Sci.(3000-3005)
11. A New High Resolution PET scanner dedicated to brain research. M.Watanabe et al. (2002) IEEE Trans. Nucl. Sci. 49(634-639)
12. The ECAT HRRT : Performance and First Clinical Application of the New High Resolution Research Tomograph. K.Wienhard et al. (2002) IEEE Trans. Nucl. Sci. 49 (104-110)
13. The ECAT HRRT : NEMA NEC Evaluation of the HRRT system – The New High Resolution Research Tomograph. K.Wienhard et al. (2002) IEEE Trans. Nucl. Sci.?
14. Performance evaluation of a new LSO High Resolution. Research Tomograph HRRT M.Schmandt et al. (1999) IEEE Trans. Nucl. Sci
15. Development of a 3-D Detector System for Positron CT K.Shimizu et al. (1988) IEEE Trans. Nucl. Sci Vol. 34, No. 1 (717-720)
16. Feasibility of a novel design of high resolution parallax-free Compton enhanced PET scanner dedicated to brain research. A.Braem et al. (2003) Proceedings Badajoz Conference (Spain)
17. High resolution 3D brain PET with hybrid photon detector. M.Chamizo Llatas (2003) Proceedings Como conference, World Scientific, in press.
18. Novel design of parallax free Compton enhanced PET scanner. A.Braem et al. (2003) Proceedings Imaging 2003 conference Stockolm (Sweden) NIM A, in press.
19. Scintillation crystals for PET. C.L Melcher (2000) J. Nucl. Medecine 41(1051-1055)
20. The evolution of scintillating medical detectors. E. Hell et al. (2000) NIM A 454 (40- 48)
21. New inorganic scintillators - aspects and energy resolution. Carel W.E Van Eijk (2001) NIM A 471 (244-248)
22. Light output and energy resolution of Ce3+ doped scintillators. P.Dorenbos (2002) NIM A 486 (208-213)
23. Current trends in scintillator detectors and materials. W.W Moses (2002) NIM A 487 (123-128)
24. Inorganic scintillators in medical imaging detectors. C.W.E Van Eijk (2003) NIM A 509

(17-25)
25. Dual APD Array readout of LSO crystals: optimization of crystal surface treatment. Y.Shao et al. (2002) IEEE Trans. Nucl. 49 (649-654)
26. Investigation of Lanthanum scintillators for 3D – PET. G. Surti et al (2003) IEEE Trans. Nucl. Sci. 50 (348-354)
27. Scintillation properties of LaBr3:Ce3+ crystal: fast, efficient and high energy resolution scintillators. E.V.D Van Loef et al. (2002) NIM A 486 (254-258)
28. E.V.D Van Loef et al. (2003) NIM A 496 (138-145)
29. LaCl3:Ce3+ scintillator for gamma ray detection. K.S Shah (2003) NIM A, in press
30. Potential of existing growth methods of LuAP and related scintillators. A.G Petrosyan et al (2002) NIM A 486 (74-78) and ref. therin
31. Hybrid Photodiodes. C. Joram Nucl. Pyhs. B (Proc. Suppl.) 78 (1999) 407
32. Hybrid photon detectors. C. DAmbrosio. H.Leutz (2003) NIM A 501 (463-498)
33. HPD and MAPMT – Segmented Photon Detectors for HEP and Beyond. C.Joram Proceedings workshop on Innovative Detectors For Supercolliders. Erice, Sicily (Italy) 4-10 Oct. 2003 World Scientific (in press)
34. Advance in Avalanche Photodiodes. Y. Musienko (2003) Proceedings. Workshop on Innovative Detectors for supercolliders Erice, Sicily (Italy), 3-10 Oct. 2003, World Scientific (in press)
35. Properties of avalanche photodiodes for applications in high energy physics, astrophysics and medical imaging. D.Renker (2002) NIM A 486 (164-169)
36. Avalanche photodiodes arrays. R.Farrell et al. (2000) NIM A 442 (171)
37. APD arrays for High Resolution PET. K.S Shah et al., SPIE, 44th Annual Meeting, July 28-23, 1999
38. Hamamatsu S 8550 APD arrays for high resolution scintillator matrix readout. M.Kaputsa et al. (2003) NIM A 504 (139-142
39. A novel photodiode array structure for gamma camera applications. O. Evrard et al. (2003) NIM A 504 (188-193)
40. Reverse APD. R. Lecomte et al. (1999) NIM A 423 (92)
41. Excess noise factor. R.J Mc Intyre (1972) IEEE trans. ED-13 (164)
42. An Apparatus for the construction of Large Area Hybrid Photodiodes. C.Joram, Proceedings workshop on New Detectors. Erice, Sicily (Italy) 1-7 Nov. 1997 World Scientific
43. Highly segmented large area Hybrid Photodiodes with bialkali photocathodes and enclosed VLSI readout electronics. A.Braem et al. (2000) NIM A 442 (128-135)
44. Development, fabrication and test of a highly segmented Hybrid photodiode. A.Braem et al (2002) NIM A 478 (400-403)
45. Technology of photocathode production. A.Braem et al. (2003) NIM A 502 (205-210)
46. The PAD-HPD : A highly segmented Hybrid photodiode. A.Braem et al (2003) NIM A 497 (202-205)
47. Development of a 10 HPD with integrated readout electronics. A.Braem et al. (2003) NIM A 504 (19-23)
48. S. E. Derenzo, W. W. Moses, R. H. Huesman and T. F. Budinger, "Critical instrumentation issues for 2 mm resolution, high sensitivity brain PET," In Quantification of Brain Function (Edited by K. Uemura, N.A. Lassen, T. Jones, et al.), Elsevier Science Publishers, Amsterdam, The Netherlands, pp. 25-37, 1993. (LBNL-34332)
49. Refractive index and absorption length of YAP:Ce scintillation crystal ...", S. Baccaro et al., NIM A 406 (1998) 479-485
50. Measurments of the effective light absorption lengths of YAP:Ce crystals for a novel geometrical concept for PET. A.Braem et al., (2004), to be published in IEEE Trans. Nucl. Science